

Access to this work was provided by the University of Maryland, Baltimore County (UMBC) ScholarWorks@UMBC digital repository on the Maryland Shared Open Access (MD-SOAR) platform.

Please provide feedback

Please support the ScholarWorks@UMBC repository by emailing [scholarworks-group@umbc.edu](mailto:scholarworks-group@umbc.edu) and telling us what having access to this work means to you and why it's important to you. Thank you.

# Tuneable structure and magnetic properties in $\text{Fe}_{3-x}\text{V}_x\text{Ge}$ alloys

R. Mahat<sup>a,\*</sup>, Shambhu KC<sup>a</sup>, D. Wines<sup>b</sup>, F. Ersan<sup>b,c</sup>, S. Regmi<sup>a</sup>, U. Karki<sup>a</sup>, R. White<sup>d</sup>, C. Ataca<sup>b</sup>, P. Padhan<sup>e</sup>, A. Gupta<sup>f</sup> and P. LeClair<sup>a,\*\*</sup>

<sup>a</sup>Department of Physics and Astronomy, University of Alabama, Tuscaloosa AL 35487

<sup>b</sup>Department of Physics, University of Maryland Baltimore County, Baltimore MD 21250

<sup>c</sup>Department of Physics, Aydin Adnan Menderes University, Aydin 09100, Turkey

<sup>d</sup>Department of Metallurgical & Materials Engineering, University of Alabama, Tuscaloosa, AL 35487

<sup>e</sup>Department of Physics, Nanoscale Physics Laboratory, Indian Institute of Technology Madras, Chennai-600036, India

<sup>f</sup>Department of Chemistry and Biochemistry, The University of Alabama, Tuscaloosa AL 35487

## ARTICLE INFO

### Keywords:

Spintronics  
Half-metals  
Heuslers  
Ferromagnets  
Crystal structure  
Martensitic phase transformation  
Electrical conductivity  
Vickers micro hardness  
Ab initio calculations

## ABSTRACT

We report a detailed experimental and theoretical study of the effects of V substitution for Fe atom on the structural, magnetic, transport, electronic and mechanical properties of an off-stoichiometric  $\text{Fe}_{3-x}\text{V}_x\text{Ge}$  intermetallic alloy series ( $0 \leq x \leq 1$ ). Single phase microstructures are observed for  $x < 0.75$ , whereas higher V content alloys  $x \geq 0.75$  are multi-phased. Vanadium substitution is observed to induce a diffusionless martensitic phase transformation from a Heusler-like  $\text{L2}_1$  structure to hexagonal  $\text{DO}_{19}$  structure, as corroborated by Differential Scanning Calorimetry results. The vanadium substitution is also found to decrease the grain size, inhibiting the grain growth by pinning the grain boundary migration. All the alloys in the series are found to be soft ferromagnets at 5 K with saturation magnetic moment and Curie temperature decreasing as V concentration increases. The low temperature saturation magnetic moment is in close agreement with the expected Slater-Pauling values for the  $\text{L2}_1$  phases, while the hexagonal samples have markedly higher values of saturation moments. First-principle calculations agree with the experimental findings and reveal that V substitution energetically favours one of the Fe sites in  $\text{Fe}_3\text{Ge}$ . The electrical resistivity measured over the temperature range from 5 K to 400 K shows negative temperature coefficient of resistivity at high temperatures with increasing the V concentration. Relatively high mechanical hardness values are also observed, with the values increasing with increasing V content. Vanadium substitution is found to play a central role in tuning the mechanical properties, stabilising the  $\text{L2}_1$  structure, and shifting the martensitic transformation temperature to higher values from that of parent  $\text{Fe}_3\text{Ge}$ .

## 1. Introduction

Heusler alloys, first discovered by and named after Fritz Heusler in 1903 [1], are very useful for applications in information storage and spintronics as well as many other areas [2–7]. For applications in magnetism and spintronics [2], the inherently low magnetocrystalline anisotropy in cubic Heusler alloys can be limiting factor [8]. Identifying a hexagonal Heusler analogue [3] that retains half metallicity and exhibits a high magneto-crystalline anisotropy may be very attractive for applications such as perpendicular media, current perpendicular to plane giant magnetoresistance (CPP-GMR), and spin-torque-transfer RAM (STT-RAM) [9–13]. However, half-metallicity has been predicted for some Heusler analogues in the hexagonal  $\text{DO}_{19}$  ( $\text{P6}_3/\text{mmc}$ , space group no. 194 [14, 15]) crystal structure [3, 16, 17].

The intermetallic compound  $\text{Fe}_3\text{Ge}$  is well known to crystallise in two crystal structures, a cubic  $\text{L1}_2$  phase ( $\text{Pm}\bar{3}\text{m}$ , space group no. 221 [14, 15]) at low temperatures ( $< 700^\circ\text{C}$ ) and hexagonal  $\text{DO}_{19}$  phase at higher temperatures ( $> 700^\circ\text{C}$ ) [18, 19]. In this compound, the forward  $\text{L1}_2$  to  $\text{DO}_{19}$  structural transformation takes place easily but the reverse  $\text{DO}_{19}$  to  $\text{L1}_2$  transformation is difficult to achieve under normal cooling conditions, and often one retains the high temperature  $\text{DO}_{19}$  crystal structure [19–21]. A few attempts have

been made in the past on the substitution of V for Fe atom in  $\text{Fe}_3\text{Ge}$  alloy and structural transformations are studied. Nakagawa and Kanematsu [22], by means of X-ray and magnetic studies have suggested the hexagonal  $\text{DO}_{19}$  phase of parent  $\text{Fe}_3\text{Ge}$  transforms to a body centred cubic (A2) structure for  $x \geq 0.50$ . They have reported the structure to be A2 due to the absence of superlattice peaks in X-ray diffraction. However, later Beitollahi and Booth [23] have reported structure to be  $\text{L2}_1$  ( $\text{Fm}\bar{3}\text{m}$ , space group no. 225 [14, 15]) based on the presence of (111) superlattice peak in their room temperature neutron diffraction patterns for nominally single phase samples with  $x \geq 0.60$ . In spite of several investigations [22, 23] aimed at understanding the structural phase transformation, the detailed mechanisms responsible for such transformations are still far from being understood. Further, they lack any microstructural analysis. Large magneto-optical Kerr rotations have also been observed in the same system [24].

To our best knowledge, there is not yet a detailed report of the structural, magnetic, transport, and mechanical properties of  $\text{Fe}_{3-x}\text{V}_x\text{Ge}$  in the bulk form, neither experimentally nor theoretically. Previous investigations focused on substituting V in one of the Fe site in  $\text{Fe}_3\text{Ge}$  under higher temperature annealing conditions. Reports on low temperature annealing conditions are not available thus far. In this study, we have addressed different annealing conditions and systematically studied the microstructure and phase purity, magnetic prop-

\*rmahat@crimson.ua.edu

\*\*pleclair@ua.edu

ORCID(s):

erties, electrical transport, differential scanning calorimetry, and hardness in addition to structure determination to understand the structure-property relationships in this interesting family of Heusler-like compounds. Particular attention has been paid to metallography and microstructural analysis to determine which regions of the phase diagram yield single phase specimens.

## 2. Experimental details

$\text{Fe}_{3-x}\text{V}_x\text{Ge}$  ( $0 \leq x \leq 1$ ) bulk samples with  $x$  varying in the steps of 0.125, were prepared by arc melting of stoichiometric amounts of the constituents in an argon atmosphere at  $10^{-4}$  mbar (see details in Supplementary Information). Care was taken to avoid oxygen contamination. As an oxygen getter, Ti was melted inside the vacuum chamber separately before melting the compound to avoid oxygen contamination. The as-cast ingots were examined repeatedly using scanning electron microscopy (SEM) and energy dispersive X-ray spectroscopy (EDS) analysis in a JEOL 7000 Field Emission Scanning Electron Microscope (FESEM) to confirm homogeneity and correct composition. After confirming the anticipated target composition, the polycrystalline ingots were then annealed in an evacuated quartz tube at different temperatures ranging from 650°C to 1000°C for different dwell times (5 days to 25 days), and at the end of each annealing cycle, the samples were cooled slowly in the furnace to get optimum crystallisation to promote the formation of  $\text{L}_{21}$  structure.

Annealed ingots were polished for spectroscopic investigations (see details in Supplementary Information). The polishing was done, first grinding using silicon carbide abrasive discs (120 through 1200 grit size) followed by diamond suspension polishing. Colloidal silica suspension of grit size 0.02  $\mu\text{m}$  was used at last for the finest polishing. After obtaining a smooth and reflective surface, the samples were etched with Adler etchant (9 g of  $\text{CuNH}_3\text{Cl}$ , 45 g of hydrated  $\text{FeCl}_2$ , 150 mL of HCl and 75 mL of DI Water) [25]. The purpose of etching is that etchant attacks different phases present in the samples at different rates, and provides high quality surface contrast for microstructure characterisation.

The crystal structure was investigated by means of X-ray diffraction (XRD) using a Bruker D8 Discover X-ray diffractometer equipped with monochromatic  $\text{Co-K}\alpha$  ( $\lambda = 0.179$  nm) radiation. The polished samples were rotated around the  $\phi$  axis during the XRD measurement to minimise surface effects. *CarIne* crystallography 4.0 software [26] as well as in-house PYTHON code [27] including the dispersive corrections to the atomic scattering factors were used to simulate the XRD patterns to compare with the experimental XRD patterns. XRD analysis (Rietveld refinement) was done using the CRYSTAL IMPACT MATCH! software based on the FULLPROF algorithm [28] that uses the least-square refinement between experimental and calculated intensities. The crystal structures determined from XRD were further confirmed using electron backscatter diffraction (EBSD) phase mapping analysis in a JEOL 7000 FESEM system.

The low temperature magnetic and electrical transport properties were studied in Quantum Design Physical Properties Measurement System (PPMS), while the high temperature magnetisation was measured using the Lakeshore VSM 7410. DSC measurements were carried out to confirm the diffusionless martensitic transformation (with a ramp rate 10°C/min during heating and cooling) in the temperature range up to 1200°C in a Setaram Labsys Evo. in Ar gas flux at the rate of 20 mL/min to prevent the possible oxidation of the samples. The temperature and the heat reaction were calibrated using high purity indium, aluminium, silver and nickel standards. The mechanical properties were studied in terms of Vicker's hardness by using Buehler model 1600-6100 micro-hardness tester.

## 3. Experimental Results and Discussions

### 3.1. Microstructural and Compositional analysis

XRD is not always sufficient to confirm the phase purity if the impurity phase content is less than 5% of the overall volume [29, 30]. In such case, optical microscopy and SEM of polished and etched samples are the most direct ways to characterise micro-structure by revealing grain boundaries, phase boundaries, and inclusion distribution. Observing different contrast in etched sample seen from optical microscopy, we can speculate the presence of impurity phases, and SEM with EDS/EBSD can be used to directly quantify whether areas of different contrast represent impurity phases or possible different crystallite orientations.

Starting from the fully stoichiometric  $\text{Fe}_2\text{VGe}$ , multiphase microstructure was obtained in every heat treatment performed at 800, 900, 950, or 1000°C for different dwelling times; 3, 5, 7, or 14 days. However, with the substitution of Fe for V, the secondary phase began to disappear and uniform single phase behaviour was observed in the V composition range ( $0 \leq x \leq 0.625$ ). All other higher V concentration produced multiphase behaviour (see details in Supplementary Information). FIG 1 shows microstructure of all single phase samples observed under high temperature annealing conditions *i.e.*, 7 days at 950°C using optical microscope. The microstructure of the high temperature ( $> 700^\circ\text{C}$ ) phase for  $x = 0$  *i.e.*, the parent  $\text{Fe}_3\text{Ge}$  compound is also presented in FIG 1 already known to be stable, annealed under similar conditions [19–21].

In addition to high temperature annealing, we also attempted to investigate low temperature annealing of our V-substituted alloys (see details in Supplementary Information) to check if the samples which showed single phase microstructure at high temperature annealing conditions were indeed stable at low temperature as well, as low temperature annealing is missing in previous works. Low temperature annealing is also necessary to shed more light on the structural phase transformation as this alloy series is reported to show structural phase transformation from low temperature  $\text{L}_{12}$  or  $\text{L}_{21}$  to high temperature  $\text{DO}_{19}$  phase, similar to parent  $\text{Fe}_3\text{Ge}$  [19–21]. Single phase granular microstructures was observed for the intermediate compositions  $x = 0.50$  and 0.25. In the case of  $\text{Fe}_3\text{Ge}$  ( $x = 0$ ), small amounts of



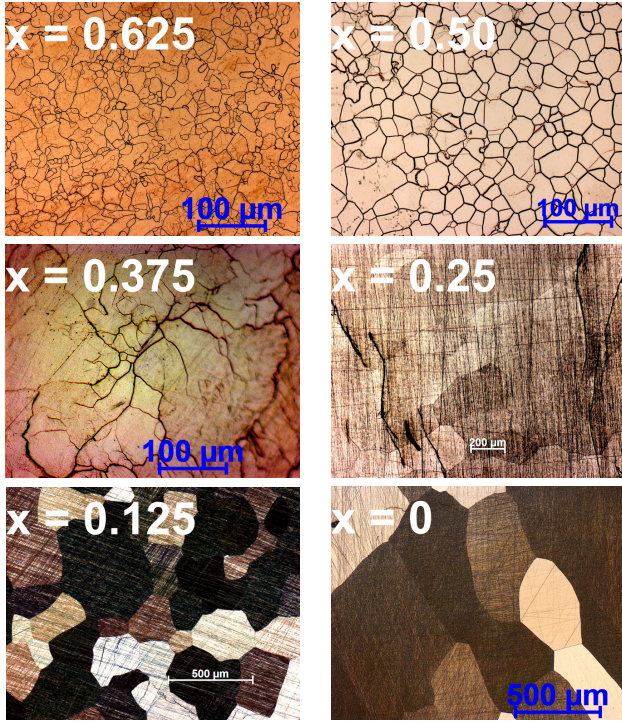


**Figure 1:** (colour online) Optical micrograph of  $\text{Fe}_{3-x}\text{V}_x\text{Ge}$  ( $0 \leq x \leq 1$ ) heat treated at  $950^\circ\text{C}$  for 7 days showing the grain structures. The samples were etched for 25 seconds using the Adler etchant.

secondary phases were observed in agreement with detailed studies on the parent  $\text{Fe}_3\text{Ge}$  compound [8, 20, 22].

The composition of all the stable single phase samples in the series are confirmed to be close to the target composition within  $\sim 5\%$  instrumental uncertainty range using EDS (see details in Supplementary Information). FIG 2 shows the SEM images displaying the microstructure of all single phase samples (see Supplementary Information for SEM images of low temperature annealed samples). Relatively small grains are observed compared to high temperature annealed samples. The effect of V substitution on the microstructure is substantial. The average grain size is observed to decrease dramatically with increasing the V content indicating the V substitution can effectively inhibit the grain boundary migration. The dramatic increase in grain size with decreasing V content is also accompanied by the increase of roughness of certain grains, producing different color contrast between neighbouring grains in bright-field as reported in the literatures [31, 32].

### 3.2. Crystal structure and atomic order analysis

FIG 3(a) shows the XRD patterns of the  $\text{Fe}_{3-x}\text{V}_x\text{Ge}$  alloy series annealed at  $950^\circ\text{C}$  for 7 days after polishing and etching, using a  $\text{Co-K}\alpha$  radiation source. The crystal structure obtained from the XRD data suggests the presence of  $\text{L}_{21}$  Heusler structure for  $0.375 \leq x \leq 0.75$  and hexagonal  $\text{DO}_{19}$  structure for  $0 \leq x \leq 0.25$ , whereas the intermediate composition  $\text{Fe}_{2.6875}\text{V}_{0.3125}\text{Ge}$  showed the co-existence of both phases and onset of structural phase transformation

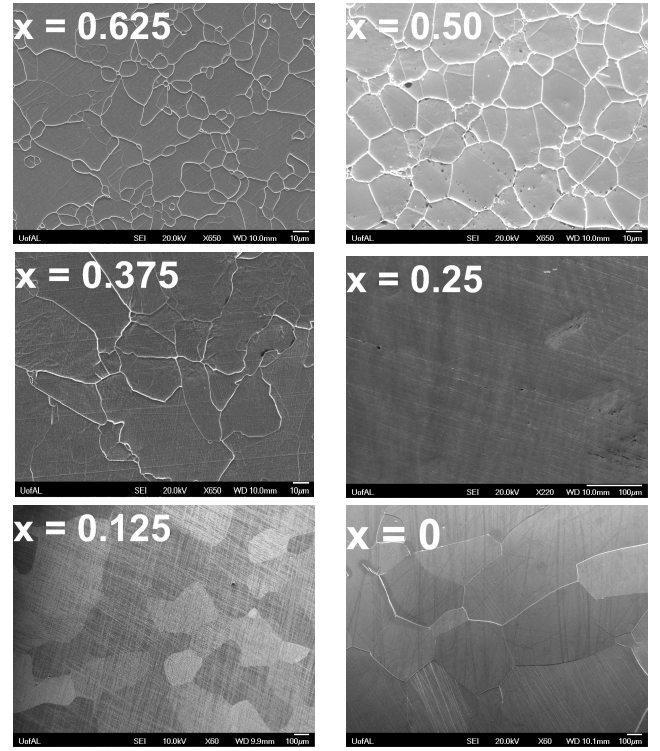


**Figure 2:** (color online) SEM micrograph of  $\text{Fe}_{3-x}\text{V}_x\text{Ge}$  ( $0 \leq x \leq 1$ ) heat treated at  $950^\circ\text{C}$  for 7 days showing the granular microstructure. The magnification of each micrograph is indicated at the bottom, like  $\times 650$  for  $x = 0.50$ .

(see FIG 3(a) fourth row from the top). FIG 3(c) shows the XRD pattern of  $\text{Fe}_{3-x}\text{V}_x\text{Ge}$  alloys series annealed at  $650^\circ\text{C}$  for 25 days. Interestingly, for the lower temperature annealing it showed Heusler like  $\text{L}_{21}$  ordering for  $x = 0.25$ , while at higher temperature annealing it showed  $\text{DO}_{19}$  ordering. The low temperature cubic  $\text{L}_{12}$  crystal phase of the parent  $\text{Fe}_3\text{Ge}$  compound is also observed with some impurity peaks (represented by asterisks) with lattice constant  $a = 3.6667 \text{ \AA}$  as reported in the literature [33].

For all cubic single-phase compositions  $0.375 \leq x \leq 0.75$ , only three distinct Heusler-like reflection peaks ( $h, k, l$  all odd or even) are observed; fundamental peaks with  $h + k + l = 4n$ , even superlattice peaks with  $h + k + l = 4n + 2$  and odd superlattice peaks  $h + k + l = 2n + 1$ . In Heusler-like alloys, presence of (111) peak indicates the chemical ordering of atoms in octahedral positions, and (200) peak reflects the superlattice reflections due to atoms in tetrahedral positions, while (220) peak is a principal reflection. None of the low angle superlattice peaks are absent in all cubic structures which indicates a degree of sublattice ordering. No mixed odd/even indices are observed in reflection peaks indicating that all cubic samples are crystallised in the face-centred cubic Heusler-like structure. The intensity of superlattice peak (111) is greater than that of (200) peak in all stable cubic phases consistently, though as noted below texturing effects makes it difficult to rely on XRD peak intensities.



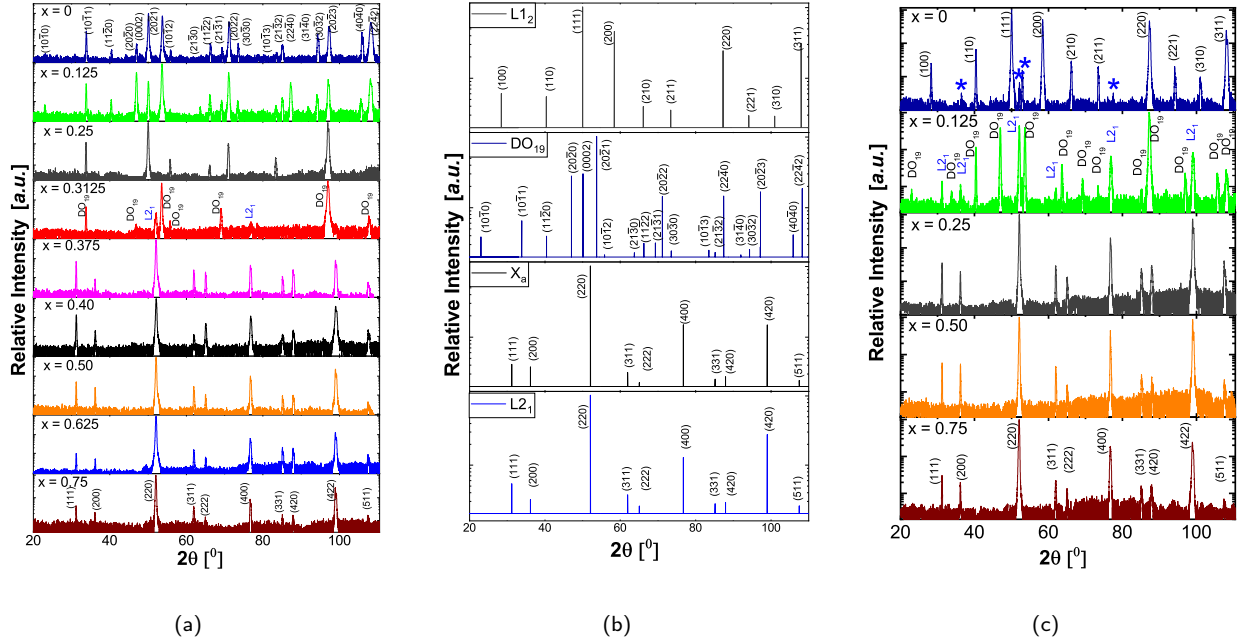


**Figure 3:** (color online) Experimental XRD patterns of  $\text{Fe}_{3-x}\text{V}_x\text{Ge}$  alloy series annealed at (a) 950°C for 7 days and (c) 650°C for 25 days using X-ray source, and (b) simulated powder XRD patterns using CaRIne. For (a), the upper indexing is for the  $\text{DO}_{19}$  structure and the lower indexing is for the  $\text{L}_{21}$  structure. For (c), the upper indexing is for the  $\text{L}_{12}$  structure and the lower indexing is for the  $\text{L}_{21}$  structure.

Considering the fact that Heusler-like compounds can crystallize in a number of structures, particularly the ordered  $\text{L}_{21}$  ( $Fm\bar{3}m$ , space group no. 225 [14, 15]) and  $\text{X}_a$  ( $F\bar{4}3m$ , space group no. 216 [14, 15]) as well as the disordered A2 and B2 phases, structure assignment should be undertaken carefully. We can argue here that there is no complete A2 and B2 disorder on the basis of presence of low angle superlattice peaks in all stable cubic compositions. Furthermore, the distinction between  $\text{L}_{21}$  and  $\text{X}_a$  structure is rather challenging from X-ray diffraction experiment if the participating elements in the alloy have similar X-ray scattering properties.

However, Beitollahi and Booth [23] previously proposed an  $\text{L}_{21}$  structure for  $x = 0.6$  to 1.0, which we corroborate here (see Table 1). Our construction of possible structures is as follows; starting from parent  $\text{Fe}_3\text{Ge}$  compound, where Fe atoms occupy 4b and 8c (or 4c and 4d) sites whereas Ge atom fills 4a site. In this picture, the substituted V atom can have several possible ways to fill the crystal structure; it can replace the Fe atom on 4b site, or 4c site, or 4d site. It is also possible for V atom to replace Ge atom to other site and fill the vacant position, however in the experimental XRD pattern we confirm that the Ge atoms form an *fcc* superstructure on the underlying *bcc* superlattice. Hence, we argue that 4a site is completely ordered. Further, the replacement of Fe atom on 4c and 4d site doesn't alter the X-ray intensity as these sites belong to the same sublattice (with octahedral symmetry). In view of this, we are left with two possibilities and we try to push further XRD based analysis to shed light

**Table 1**

Possible site assignments for cubic  $\text{Fe}_{3-x}\text{V}_x\text{Ge}$  assuming two space groups;  $\text{L}_{21}$  ( $Fm\bar{3}m$ ) and  $\text{X}_a$  ( $F\bar{4}3m$ ).

Type	Ge	$\text{Fe}_{1-x}\text{V}_x$	Fe	Fe
$\text{L}_{21}$	4a (0,0,0)	4b ( $\frac{1}{2}, \frac{1}{2}, \frac{1}{2}$ )	8c ( $\frac{1}{2}, \frac{1}{4}, \frac{1}{4}$ )	8c ( $\frac{1}{4}, \frac{1}{4}, \frac{3}{4}$ )
$\text{X}_a$	4a (0,0,0)	4c ( $\frac{1}{4}, \frac{1}{4}, \frac{1}{4}$ )	4b ( $\frac{1}{2}, \frac{1}{2}, \frac{1}{2}$ )	4d ( $\frac{3}{4}, \frac{3}{4}, \frac{3}{4}$ )

on the exact atomic order of the alloys. To further narrow down the exact atomic ordering, we simulated the XRD patterns for  $\text{Fe}_{2.50}\text{V}_{0.50}\text{Ge}$  considering different crystal structures (see FIG 3(b)). The experimental XRD pattern observed matches to  $\text{L}_{21}$  structure generated in either CaRIne 4.0 simulations or CRYSTAL IMPACT MATCH, or our in-house python code for  $\text{Fe}_{2.50}\text{V}_{0.50}\text{Ge}$ . The superlattice peaks (111) and (200) have a little bit higher intensity than those generated from simulations, which might be due to texturing effects, given the large grain size we observe ( $\sim 30 \mu\text{m}$ ). As the crystal structure of parent  $\text{Fe}_3\text{Ge}$  is hexagonal  $\text{DO}_{19}$  at higher temperature ( $> 700^\circ\text{C}$ ) and cubic ( $\text{L}_{12}$ ) at lower temperature ( $< 700^\circ\text{C}$ ), the  $\text{L}_{12}$  crystal structure was also simulated using CaRIne 4.0 software, but none of the intensities and peak positions matched with the experimental pattern (see FIG 3(b)).

Rietveld refinement shows good agreement (reduced  $\chi^2 = 1.4$  and weighted average Bragg  $R$ -factor = 3.6) between the observed XRD pattern and the calculated pattern for the  $\text{L}_{21}$  (space group 225) structure with the experimental lattice

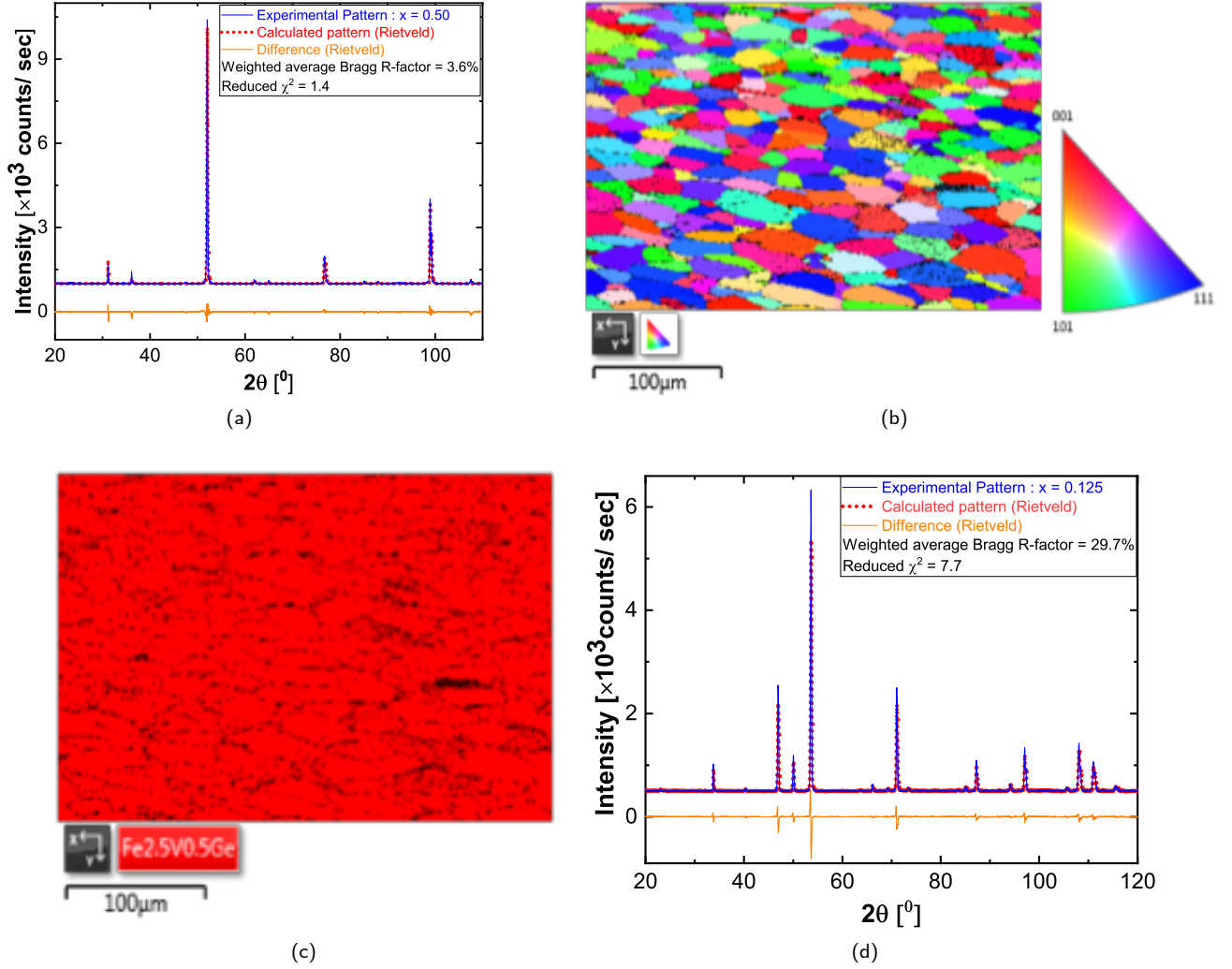


**Figure 4:** (color online) (a) The Rietveld refinement of XRD pattern showing a signature of good fit with the proposed crystal model  $\text{L2}_1$  (b) IPF color map (c) The corresponding EBSD phase color map of the same area of  $\text{Fe}_{2.50}\text{V}_{0.50}\text{Ge}$  in SEM (d) The Rietveld refinement of XRD pattern for  $\text{Fe}_{2.875}\text{V}_{0.125}\text{Ge}$  with the proposed  $\text{DO}_{19}$  crystal structure.

**Table 2**

Proposed site assignment for the hexagonal  $\text{DO}_{19}$   $\text{Fe}_{3-x}\text{V}_x\text{Ge}$ .

	Wyckoff position	Coordinates	Occupancy
Fe	$6h, y = \frac{5}{6}$	$(y, 2y, \frac{1}{4}) (-2y, -y, \frac{1}{4}) (y, -y, \frac{1}{4}) (-y, -2y, \frac{3}{4}) (2y, y, \frac{3}{4}) (-y, y, \frac{3}{4})$	$\frac{3-x}{3}$
V	$6h, y = \frac{1}{6}$	$(y, 2y, \frac{1}{4}) (-2y, -y, \frac{1}{4}) (y, -y, \frac{1}{4}) (-y, -2y, \frac{3}{4}) (2y, y, \frac{3}{4}) (-y, y, \frac{3}{4})$	$\frac{x}{3}$
Ge	$2c$	$(\frac{1}{3}, \frac{2}{3}, \frac{1}{4}) (\frac{2}{3}, \frac{1}{3}, \frac{3}{4})$	1

parameter  $a = 5.7632 \text{ \AA}$  as shown in FIG 4(a). The goodness of fit parameters (reduced  $\chi^2 = 5.2$  and weighted average Bragg  $R$ -factor = 9.7) are always higher for  $X_a$  (space group 216) structure considered in Table 1. Having no evidence to the contrary, we presume Fe and V mix randomly on the 4b sites. This is also in good agreement with the Pauling electronegativity rule. Because V and Ge have a higher electronegativity difference, they will tend to form a rock-salt (NaCl) type lattice and coordinate octahedrally due to ionic nature of their interactions. EBSD inverse pole figure (IPF)

map and phase map of  $\text{Fe}_{2.50}\text{V}_{0.50}\text{Ge}$  were also performed to determine the degree of texturing and purity of phase considered. Relatively large grains with some preferred orientation is revealed from IPF as shown in FIG 4(b). Almost 95% of the selected microstructure is observed to match the proposed  $\text{L2}_1$  structure (red color in the EBSD map (see FIG 4(c)) with some zero solution regions (black spots) mainly in grain boundaries due to the artefact of polishing and some nominal Ge segregation. All these experimentally observed facts support that the crystal structure of all stable cubic sam-

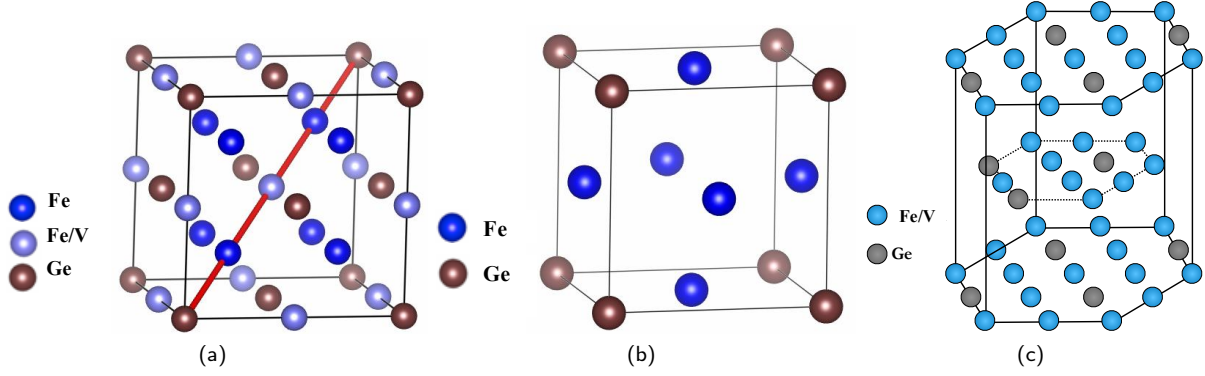


**Figure 5:** (color online) Various crystal structures (a)  $\text{L}_{21}$ , (b)  $\text{L}_{12}$ , and (c)  $\text{DO}_{19}$

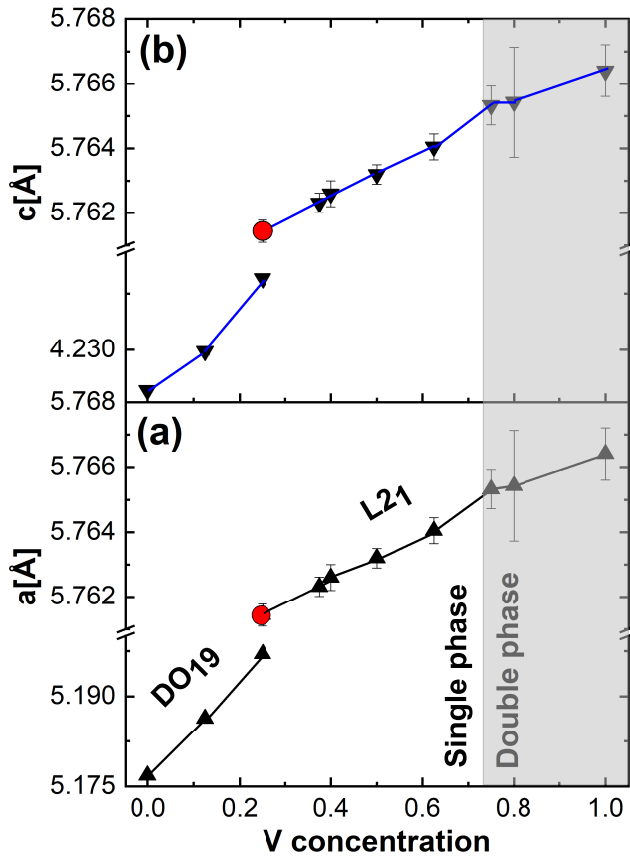


**Figure 6:** (color online) Variation of lattice parameters of  $\text{Fe}_{3-x}\text{V}_x\text{Ge}$  annealed at  $950^\circ\text{C}$  for 7 days (except the red data point representing  $x = 0.25$  annealed at  $650^\circ\text{C}$  for 25 days) (a)  $a$  versus V concentration, and (b)  $c$  versus V concentration. The shaded region represents multiphase region.

ples  $0.375 \leq x \leq 0.75$  is  $\text{L}_{21}$ , in agreement with Beitollahi and Booth [23]. The  $\text{L}_{21}$  structure is shown in FIG 5(a).

In order to determine the atomic ordering in hexagonal samples,  $x = 0.125$  is chosen for Rietveld refinement due to the visibility of all hexagonal peaks in XRD. Even though the texturing effect from larger grains ( $\sim 300 \mu\text{m}$ ) is evident

in peak intensities, a final reduced  $\chi^2 = 7.7$  is found. This single digit goodness of fit parameter between the observed XRD pattern and the calculated pattern for the hexagonal  $\text{DO}_{19}$  (space group 194) indicates the reliability of the fit (see FIG 4(d)). According to Rietveld refinement, the 6h sites (with the parameter  $y = 5/6$ ) are shared by Fe and V with occupancy 0.958 and 0.042, respectively, in agreement with the nominal composition, and the 2c sites are occupied by Ge. Again, with no evidence to the contrary, we presume that Fe and V mix randomly on the 6h sites. This  $\text{DO}_{19}$  structure is shown in FIG 5(c). The proposed site assignments are summarised for  $\text{DO}_{19} \text{Fe}_{3-x}\text{V}_x\text{Ge}$  in Table 2 [17].

Lattice parameters of all cubic stable phases, calculated using Cohen's method with a Nelson-Riley error function [34], are observed to increase linearly with increasing V concentration (see FIG 6(c)) which is expected according to Vegard's law [35] as the lattice constant of bcc V (0.3024 nm) is greater than that of bcc Fe (0.2867 nm) [36]. Both lattice parameters  $a$  and  $c$  increase with the increase of V concentration for all hexagonal stable phases as shown in FIG 6. The lattice parameters of all stable samples along with different annealing conditions for  $\text{Fe}_{3-x}\text{V}_x\text{Ge}$  alloy series are presented in Table 3.

### 3.3. Phase transformation behaviour and thermal stability

Differential Scanning Calorimetry (DSC) is a simple but an effective tool to identify phase transformation temperatures. Since the local composition of our samples does not change in going from one structure to another, this serves to indicate that the transformation is a diffusionless martensitic transformation, as observed in the parent compound  $\text{Fe}_3\text{Ge}$ . Continuous heating and cooling DSC curves of  $\text{Fe}_{3-x}\text{V}_x\text{Ge}$  annealed at  $950^\circ\text{C}$  for 7 days measured at a heating/cooling rate of  $10^\circ\text{C}/\text{min}$  are shown in FIG 7(a). FIG 7(b) shows the DSC curves at heating/cooling rate  $10^\circ\text{C}/\text{min}$  for  $x = 0$  and  $x = 0.25$  annealed at  $650^\circ\text{C}$  for 25 days. The phase evolution is clearly seen from the DSC curves. The large, sharp endothermic peaks around  $1120^\circ\text{C}$  corresponds to the melting point which is in agreement with the reported melting point  $\sim 1100^\circ\text{C}$  of parent  $\text{Fe}_3\text{Ge}$ . Additionally, small endothermic



**Table 3**

Experimental lattice parameters of  $\text{Fe}_{3-x}\text{V}_x\text{Ge}$  alloy series of different crystal structures with annealing conditions, the experimental saturation magnetic moments at  $T = 5\text{ K}$  along with the theoretical and Slater-Pauling (S-P) values, and the measured Curie temperature ( $T_c$ ). The numbers in parentheses are the uncertainty in the last digit, e.g.,  $3.2(2) = 3.2 \pm 0.2$ .

$x$	Crystal structure	Experimental lattice (Å)	Theoretical lattice (Å)	Expt. $M_s$ at $T = 5\text{ K}$ ( $\mu_B/f.u.$ )	Theor. $M_s$ ( $\mu_B/f.u.$ )	S-P $M_s$ ( $\mu_B/f.u.$ )	$T_c$ (K)
0	$\text{DO}_{19}^\dagger$	$a = 5.1768(2)$ $c = 4.2246(3)$	$a = 5.134$ $c = 4.222$	6.55(9)	6.48	4.00	640
0	$\text{L1}_2^{*\dagger}$	$a = 3.6667(1)$	$a = 3.638$	6.55(9)	6.45	4.00	-
0.125	$\text{DO}_{19}^\dagger$	$a = 5.1863(5)$ $c = 4.2298(5)$	$a = 5.146$ $c = 4.220$	5.88(2)	6.07	3.63	620(10)
0.125	$\text{L2}_1 + \text{DO}_{19}^{*\dagger}$	-	-	-	-	-	-
0.25	$\text{DO}_{19}$	$a = 5.1970(4)$ $c = 4.2395(3)$	$a = 5.159$ $c = 4.220$	5.33(3)	5.72	3.25	603(12)
0.25	$\text{L2}_1^\ddagger$	$a = 5.7614(3)$	$a = 5.753$	3.91(3)	3.77	3.25	-
0.375	$\text{L2}_1^\ddagger$	$a = 5.7623(3)$	$a = 5.767$	3.18(2)	-	2.88	590(9)
0.40	$\text{L2}_1^\ddagger$	$a = 5.7626(1)$	-	3.09(3)	-	2.80	-
0.50	$\text{L2}_1^\ddagger$	$a = 5.7632(3)$	$a = 5.788$	2.64(3)	2.47	2.50	509(8)
0.625	$\text{L2}_1^\ddagger$	$a = 5.7640(4)$	$a = 5.802$	2.24(2)	-	2.13	450(5)
0.75	$\text{L2}_1^{*\ddagger}$	$a = 5.7653(6)$	$a = 5.806$	-	1.62	1.75	-

$^\dagger$  annealed at  $950^\circ\text{C}$  for 7 days,  $^\ddagger$  annealed at  $650^\circ\text{C}$  for 25 days, \* multi-phased samples.

peaks are seen in addition to the prominent melting point peaks for all compositions having  $\text{L2}_1$  structures, indicating the signature of first order phase transformations.

No peaks are observed in those compositions which were already crystallised in hexagonal  $\text{DO}_{19}$  structure at room temperature. Small endothermic peaks are also observed for  $x = 0$  ( $\text{L1}_2$ ) and  $x = 0.25$  ( $\text{L2}_1$ ) annealed at  $650^\circ\text{C}$  for 25 days during heating cycle only. All these experimentally observed facts indicate that transforming the  $\text{L1}_2$  or  $\text{L2}_1$  structure to the  $\text{DO}_{19}$  structure is relatively easy, but the reverse transition is relatively difficult for low V concentration [19, 20]. Additionally, XRD on samples with  $x = 0.25$  annealed at  $950^\circ\text{C}$  for 7 days and at  $650^\circ\text{C}$  for 25 days showed a  $\text{DO}_{19}$  structure and a  $\text{L2}_1$  structure, respectively, corroborating the DSC measurements. Thus, we conclude that the small DSC peaks observed correspond to the structural phase transformation from cubic  $\text{L1}_2$  or  $\text{L2}_1$  to hexagonal  $\text{DO}_{19}$ . The linear shifting of the peak positions with increasing vanadium concentration, as shown in FIG 7(c), indicates an improvement of the stability of the low temperature  $\text{L2}_1$  structure with increasing V content. Notably, this low temperature  $\text{L2}_1$  phase with V substitution is completely different from the low temperature  $\text{L1}_2$  phase of the parent  $\text{Fe}_3\text{Ge}$ . The reproducibility of those peaks on cooling (with some hysteresis) and the lack of local composition variation suggests the transformation to be of the diffusionless martensitic type. We note that the hysteresis may be due to super-cooling (recall the heating/cooling rate of  $10^\circ\text{C}/\text{min}$ ). The total entropy of phase transformation also changes significantly with V concentration (see FIG 7(d)).

The onset temperatures ( $T_1$ ), temperatures ( $T_p$ ) and total entropy change ( $\Delta S_p$ ) of the phase transformation peaks, and melting points ( $T_m$ ), measured at heating rate  $10^\circ\text{C}/\text{min}$  for samples annealed at  $950^\circ\text{C}$  for 7 days with different vana-

**Table 4**

The values  $T_1$ ,  $T_p$ ,  $\Delta S_p$ , and  $T_m$  of  $\text{Fe}_{3-x}\text{V}_x\text{Ge}$  annealed at  $950^\circ\text{C}$  for 7 days measured in continuous heating at the rate  $10^\circ\text{C}/\text{min}$ . (The subscripts 1,  $p$  and  $m$  denote for on-set,  $\text{L2}_1$  to  $\text{DO}_{19}$  transformation, and melting point, respectively.) The numbers in parentheses are the uncertainty in the last digit.

$x$	$T_1(^{\circ}\text{C})$	$T_p(^{\circ}\text{C})$	$\Delta S_p (\text{J/g}\cdot\text{K})$	$T_m(^{\circ}\text{C})$
0*	721	743	0.15(2)	1112
0.125	-	-	-	1115
0.25*	737	758	0.14(2)	1116
0.375	828	849	0.17(2)	1118
0.40	842	865	0.18(1)	1121
0.50	905	932	0.26(3)	1124
0.625	965	976	0.42(2)	1126

\*Samples annealed at  $650^\circ\text{C}$  for 25 days.

dium concentrations are presented in Table 4.

Thus, the  $\text{L2}_1$  to  $\text{DO}_{19}$  martensitic phase transformation is observed to depend on V concentration as well as annealing temperature conditions in off-stoichiometric  $\text{Fe}_{3-x}\text{V}_x\text{Ge}$  intermetallic alloys, distinct from the temperature driven  $\text{L1}_2$  to  $\text{DO}_{19}$  transformation of the parent compound  $\text{Fe}_3\text{Ge}$ . After annealing at  $950^\circ\text{C}$  for 7 days, alloys for  $0.375 \leq x \leq 0.75$  are found to crystallize in the Heusler-like  $\text{L2}_1$  structure, and alloys with  $0 \leq x \leq 0.25$ , crystallize in the hexagonal  $\text{DO}_{19}$  structure, which is the high temperature structure of the parent  $\text{Fe}_3\text{Ge}$ . On the other hand, alloys with  $0.25 \leq x \leq 0.75$  annealed at  $650^\circ\text{C}$  for 25 days are observed to crystallize in  $\text{L2}_1$  structure. Clearly two distinct crystal structures are observed at room temperatures in  $x = 0.25$ ;  $\text{L2}_1$  for sample annealed at  $650^\circ\text{C}$  for 25 days and  $\text{DO}_{19}$  for sample annealed at  $950^\circ\text{C}$  for 7 days, confirming the  $\text{L2}_1$  to  $\text{DO}_{19}$  *fcc* to *hcp* phase transformation, likely similar to those widely studied in cobalt and ferrous alloys [37, 38].

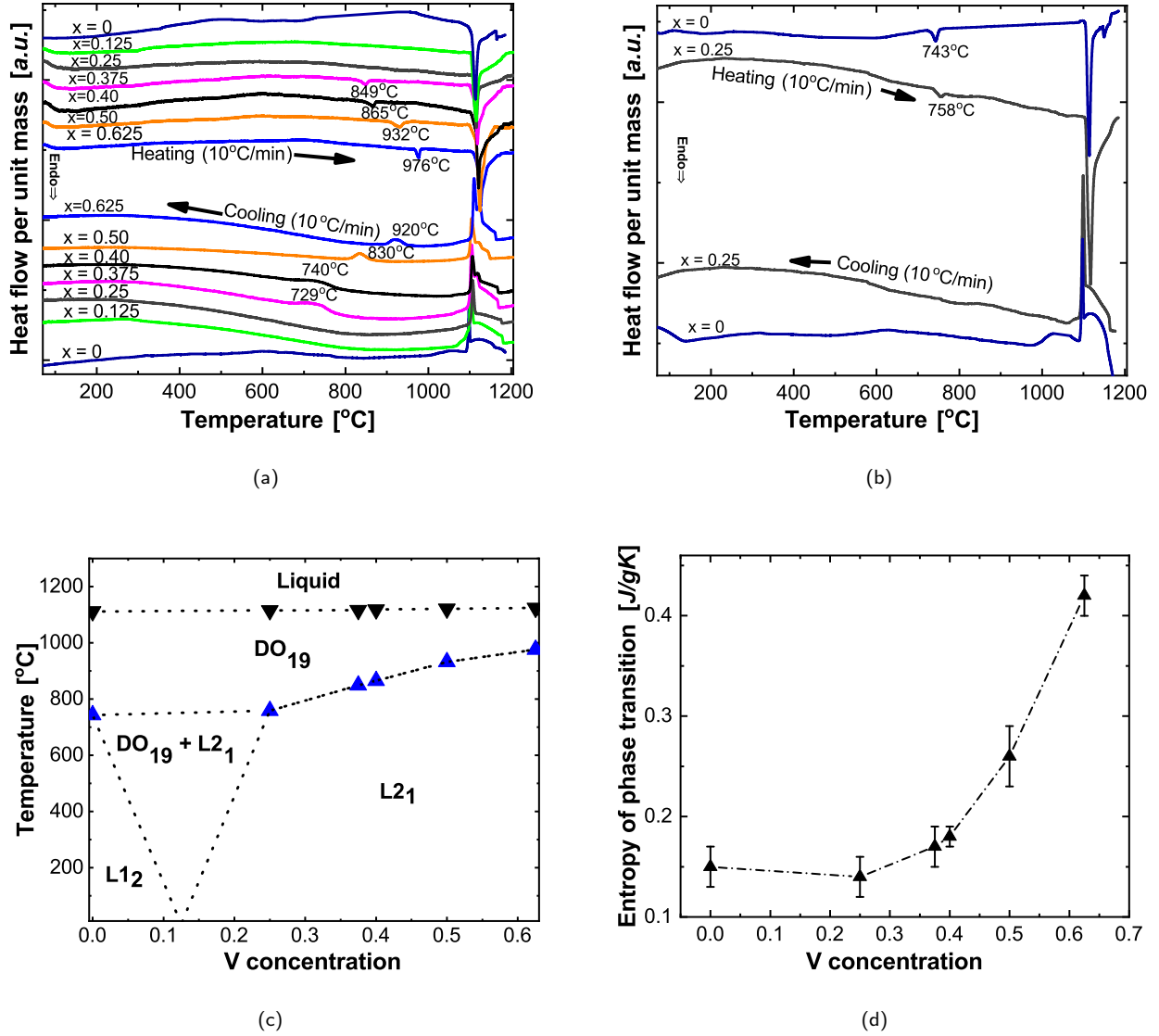


**Figure 7:** (color online) (a) DSC scans of  $\text{Fe}_{3-x}\text{V}_x\text{Ge}$  alloy series heat-treated at 950°C for 7 days measured at heating/cooling rate 10°C/min. (b) DSC scans for  $x = 0$  and  $x = 0.25$  heat-treated at 650°C for 25 days at heating/cooling rate 10°C/min. (c) Temperature versus V concentration phase diagram of  $\text{Fe}_{3-x}\text{V}_x\text{Ge}$  alloy system. Martensitic phase transformation temperature: blue data points, Melting point: red data points, and dashed lines: proposed phase boundaries. (d) The total entropy of phase transformation with V concentration.

According to the Shoji-Nishiyama mechanism, the atomic arrangements of the  $(111)_{fcc}$  plane and the  $(0001)_{hcp}$  planes are parallel [37]. Since, both *fcc* and *hcp* are close-packed structures, the only difference is in the stacking sequence of atoms normal to these planes. The transformation from *fcc* to *hcp* only requires the deformation of the atoms along the  $(111)$  plane to form a stacking sequence from *ABCABC* ... to *ABABA* ... type [39].

### 3.4. Magnetic Characterisation

The magnetic measurements for all single-phase samples were done using the VSM module of a Quantum design PPMS Dynacool. FIG 8(a) shows the field dependent mag-

netisation  $M(H)$  curves of all stable samples in the  $\text{Fe}_{3-x}\text{V}_x\text{Ge}$  series at 5 K. All the samples appeared to be ferromagnetic at 5 K. The saturation magnetising field is observed to decrease with increasing V content, though all samples are magnetically very soft. The saturation magnetic moments ( $M_s$ ) were extracted from an Arrot plot [41], *i.e.*, by extrapolating the linear part of  $M^2$  versus to  $H/M$  to  $H/M = 0$  (see inset to FIG 8(a)). The extracted  $M_s$  at 5 K is observed to decrease linearly with increasing V content, however two different trendlines are observed (see FIG 8(b)). This anomaly can be attributed due to different crystal structures (DO<sub>19</sub> structure for low V content and L2<sub>1</sub> for high V content) consistent with our microstructural and XRD analysis. The ex-

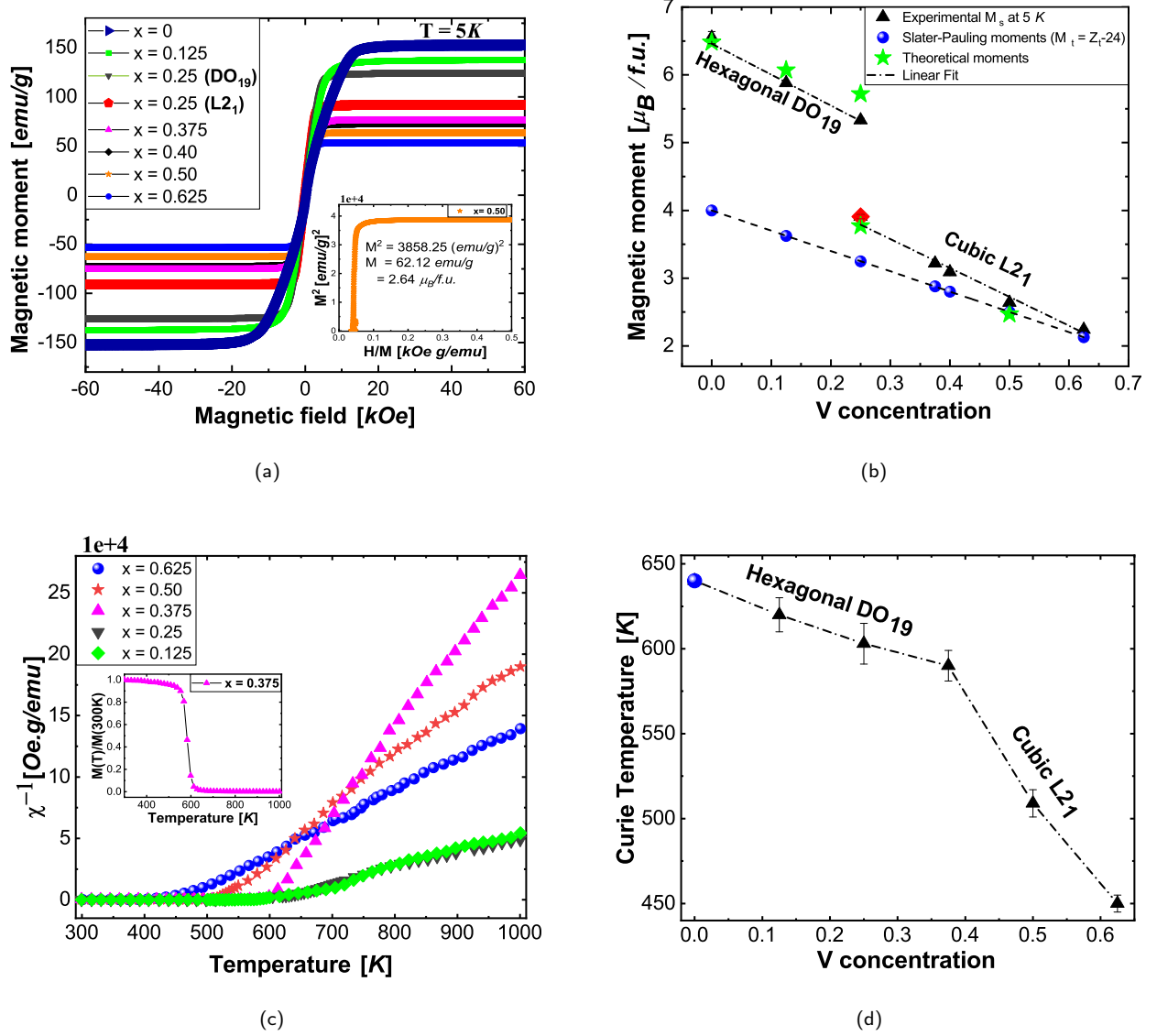


**Figure 8:** (color online) (a) The field-dependent magnetisation at 5 K of  $\text{Fe}_{3-x}\text{V}_x\text{Ge}$  alloy series annealed at 950°C for 7 days except the sample  $x = 0.25 (\text{L2}_1)$  which was annealed at 650°C for 25 days. The inset indicates the Arrot plot. (b) The magnetic moment versus V concentration both experimental and expected from Slater Pauling rule. (c) Inverse susceptibility as a function of temperature for the alloys ( $0.125 \leq x \leq 0.625$ ) annealed at 950°C for 7 days. The inset is temperature dependent magnetisation for  $x = 0.375$  with  $H = 1000 \text{ Oe}$ . (d) The variation of  $T_c$  with V concentration (The blue data point is literature value of parent  $\text{Fe}_3\text{Ge}$  [21, 40]).

tracted values of saturation magnetic moment ( $M_s$ ) versus V concentration plot presented in FIG 8(b) shows linear behaviour for all stable  $\text{L2}_1$  phases, in good agreement with Slater-Pauling rule (shown in blue data points). The Slater-Pauling rule describes the dependence of the magnetic moment on the valence electron concentration ( $N_v$ ) for ordered, half-metallic ferromagnetic Heusler compounds. This dependence is given by [4]

$$m = N_v - 24. \quad (1)$$

The slightly higher extracted saturation magnetic moments in the Fe rich members of  $\text{L2}_1$  series are not unusual. Similar deviations from the theoretical values have been reported previously for Fe based Heusler compounds elsewhere [4, 42]. The plot also shows linear behaviour for  $\text{DO}_{19}$  compositions, but the values are much higher than values from Slater-Pauling rule which simply indicates that the Slater-Pauling rule is not expected to hold for the hexagonal structure. Dramatic changes in magnetic moment are observed at  $x = 0.25$  depending on the annealing condition, where we clearly observed two distinct pure crystal structures,  $\text{DO}_{19}$



for sample annealed at 950°C for 7 days and  $L2_1$  for sample annealed at 650°C for 25 days. The red coloured solid square data point in FIG 8(b) represents the magnetic moment for  $x = 0.25$  ( $L2_1$ ) annealed at 650°C for 25 days. All experimentally extracted saturation magnetic moments are in good agreement with those obtained from first-principle calculations (see FIG 8(b)) (discussed in theory section below).

The high temperature magnetisation of a series of heat-treated  $\text{Fe}_{3-x}\text{V}_x\text{Ge}$  alloy were measured by means of a vibrating sample magnetometer VSM equipped with a high temperature stage. The Curie temperatures of intermetallic alloy series were extracted taking the average of values obtained from linear fitting of the inverse susceptibility versus temperature graph as shown in FIG 8(c) and the values obtained by plotting  $dM/dT$  as a function of temperature. The inset in FIG 8(c) shows the specific magnetisation as a function of temperature for  $x = 0.375$ . The measurements were performed with a constant magnetic field of 1000 Oe in the temperature range of 300 K to 1000 K. Even though the ferromagnetic Curie temperature  $T_c$  of these alloys are all observed to be above room temperature, and decrease with increasing  $x$  as shown in FIG 8(d), the linear decrease of  $T_c$  of hexagonal samples  $x = 0.125$  and  $x = 0.25$  has different slope than that of cubic ones. The  $T_c$  values are well below the melting point and martensitic phase transition temperatures obtained by means of differential scanning calorimetry.

The saturation magnetic moments at 5 K and corresponding Curie temperature of all stable samples along with different annealing conditions for  $\text{Fe}_{3-x}\text{V}_x\text{Ge}$  alloy series are presented in Table 3 above.

### 3.5. Electrical resistivity

The electrical resistivity data were collected using the van der Pauw method [43] in a PPMS Dynacool for samples with approximate dimensions  $4 \times 4 \times 1.5 \text{ mm}^3$ . FIG 9 shows the temperature dependence of the electrical resistivity for  $\text{Fe}_{3-x}\text{V}_x\text{Ge}$  measured during heating process in the temperature range from 5 K to 400 K. The electrical resistivity is observed to be sensitive to the composition change. An increase of V substitution for Fe is found to increase the residual resistivity that could be attributed due to atomic disorder arising from the substitution or sample quality. For  $x = 0.25$  the variation of resistivity with temperature is purely metallic (see FIG 9), but for higher V concentrations, a typical metallic behaviour is observed only for the low temperature range from 5 K up to 200 K. The resistivity is observed to saturate at higher temperatures for  $x = 0.50$ , suggesting a parallel contribution of the intrinsic resistivity and a weakly-varying shunting resistance, possibly due to grain boundaries [44, 45]. The pseudo gap near Fermi level present in the minority spin channel of total density of state (see FIG 13) for  $x = 0.50$  might be responsible for this saturation effect. According to Allen and Chakraborty [45], the resistivity of a sub-band of electrons with an energy gap at the Fermi level is high and independent of temperature while the other sub-band has metallic character and resistiv-

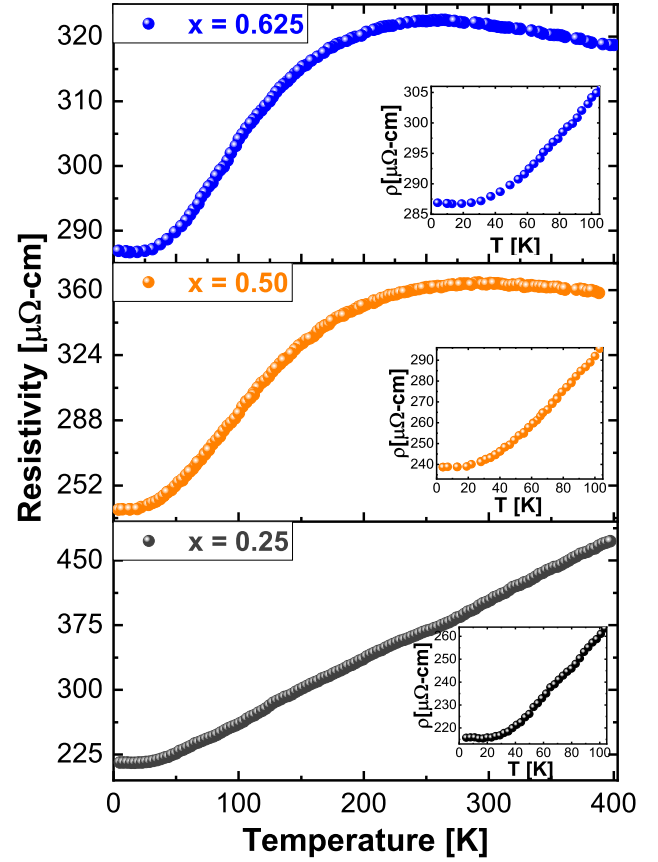


**Figure 9:** (color online) Temperature dependence of electrical resistivity in  $\text{Fe}_{3-x}\text{V}_x\text{Ge}$  ( $x = 0.25, 0.50$ , and  $0.625$ , all annealed at 950°C for 7 days respectively from bottom to top) in zero magnetic field.

ity increases with temperature and saturates at high temperature. The downturn in resistivity at higher temperature for  $x = 0.625$  indicates the semiconducting nature of the material. This kind of anomalous behaviour of resistivity is quite similar to those observed in  $\text{Fe}_{2-x}\text{V}_{1+x}\text{Al}$ ,  $\text{Fe}_{2-x}\text{Ti}_{1+x}\text{Sn}$ ,  $(\text{Fe}_{1-x}\text{V}_x)_3\text{Ga}$ , and  $(\text{Fe}_{1-x}\text{Ti}_x)_3\text{Ga}$  systems, where the tendency toward negative temperature dependence of electrical resistivity increases markedly with increasing  $x$  [46–49]. The anomaly that the resistivity reaches the maximum value quickly at  $T \leq T_c$ , decreases after that and reaches saturation at higher temperature is observed in many half-metallic Heusler alloys where the resistivity of one of the spin polarised sub-band with energy gap at Fermi level is expected to have a semiconductor character at high temperature [50–57]. The energy gap in down spin sub-band is observed to fall at Fermi level for  $x = 0.75$  (see FIG 13). The existence of a gap in one of the spin-polarised sub-band near Fermi level in total density of state for higher V concentration in  $\text{Fe}_{3-x}\text{V}_x\text{Ge}$  can be considered as the anomalous decrease of resistivity with increasing temperature. Elucidating the true bulk transport properties unambiguously would ideally require single crystal or highly ordered thin films.

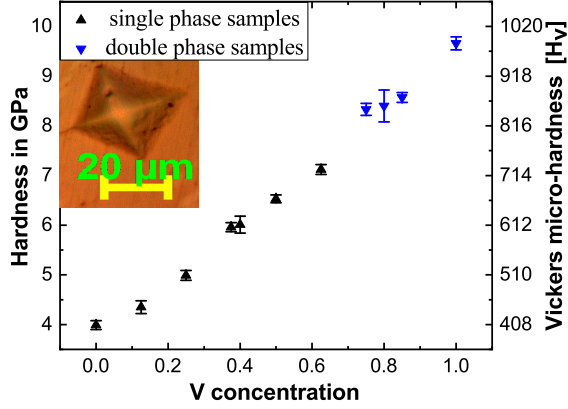


**Figure 10:** (color online) Vickers hardness versus V concentration in  $\text{Fe}_{3-x}\text{V}_x\text{Ge}$  with imprint of the indenter with radial cracks for  $x = 0$  [top left]. The black data points represent the single phase compositions.

### 3.6. Vickers micro hardness

During specimen preparation, we found the samples to be unusually hard, as evidenced by the polishing time required. For this reason, we decided to investigate the Vickers hardness of our alloy series, since most of the previous studies on mechanical properties are theoretical in nature [58–62] and only few are verified experimentally. The variation of Vickers micro hardness of our alloy series (all annealed at  $950^\circ\text{C}$  for 7 days) with V concentration is presented in FIG 10 with corresponding values in Table 5. Hardness values reported are the averages of data taken from at least 12 different regions of each sample with 0.2 kg load and 10 s loading time. Relatively high hardness values are measured, approaching 10 GPa for  $x = 1$ , comparable with highest value 12 GPa reported for  $\text{Co}_{2-x}\text{Ti}_x\text{FeGe}$  Heusler system [30] and higher than values reported for full Heuslers in the literature, e.g.,  $\sim 8.5$  GPa for powder  $\text{Fe}_2\text{VAl}$  [63],  $\sim 8.5$  GPa for nanocrystalline  $\text{Co}_2\text{FeAl}$  [64],  $\sim 7.3$  GPa and  $\sim 7.9$  GPa for bulk polycrystalline  $\text{Co}_2\text{MnGe}$  and  $\text{Co}_2\text{MnSi}$  respectively [65]. The hardness is observed to increase almost linearly in going from hexagonal  $\text{DO}_{19}$  phases (with low V concentration) to  $\text{L2}_1$  phases (with higher vanadium concentration) and depend on grains size and phases present as reported in the literature [66]. The grain size of the hexagonal phases at low V concentration are bigger than those of cubic phases at higher concentrations, and the cubic structure shows better toughness than the hexagonal structure, presumably as the *fcc* structure has more slip planes in which the atoms are packed most closely relative to each other, and hence most tightly bonded to each other [67].

**Table 5**

Vicker's micro-hardness of the  $\text{Fe}_{3-x}\text{V}_x\text{Ge}$  alloy series.

$x$	Vickers Hardness (GPa)
0	$3.99 \pm 0.09$
0.125	$4.35 \pm 0.13$
0.25	$4.99 \pm 0.10$
0.3125	$4.81 \pm 0.37$
0.375	$5.96 \pm 0.09$
0.40	$6.01 \pm 0.17$
0.50	$6.53 \pm 0.08$
0.625	$7.12 \pm 0.10$
0.75	$8.33 \pm 0.12$
0.80	$8.40 \pm 0.32$
0.85	$8.57 \pm 0.10$
1	$9.66 \pm 0.13$

## 4. Theoretical Calculations

### 4.1. Computational Methodology

The Vienna Ab initio Simulation Package (VASP) was used for our density functional theory calculations (DFT) [68]. We used potentials from the projector augmented-wave (PAW) method and used the Perdew-Burke-Ernzerhof (PBE) functional [69–71]. The Monkhorst-Pack scheme was used to sample the Brillouin zone using a  $9 \times 9 \times 9$  k-point grid for cubic structures and a  $9 \times 9 \times 5$  grid for hexagonal structures in addition to a plane wave basis set with a cutoff energy of 400 eV [72]. Self-consistent field calculations of the total and projected electronic density of states were carried out with a Gaussian-type Fermi-level smearing width of 0.05 eV. To generate  $\text{Fe}_{3-x}\text{V}_x\text{Ge}$  structures with varying V concentrations, we used the Special Quasi-random Structures (SQS) method implemented in the ATAT package [73, 74]. The formation energy  $E_{\text{form}}$  (in eV/atom) of  $\text{Fe}_{3-x}\text{V}_x\text{Ge}$  is defined as  $E_{\text{form}} = (E_{\text{Fe}_{3-x}\text{V}_x\text{Ge}} - (1-x)E_{\text{Fe}_3\text{Ge}} - xE_{\text{V}_3\text{Ge}})/3$ , where  $E_{\text{Fe}_{3-x}\text{V}_x\text{Ge}}$  is the energy of a  $\text{Fe}_{3-x}\text{V}_x\text{Ge}$  cell,  $E_{\text{Fe}_3\text{Ge}}$  is the energy of a  $\text{Fe}_3\text{Ge}$  cell, and  $E_{\text{V}_3\text{Ge}}$  is the energy of a  $\text{V}_3\text{Ge}$  cell, all per formula unit. We then normalised the x axis to start from  $x = 0$  ( $\text{Fe}_3\text{Ge}$ ) to  $x = 1$  ( $\text{Fe}_2\text{VGe}$ ). To obtain the charge distribution on the atoms in the simulation cells, we used Bader charge analysis [75, 76]. The VESTA program was used to visualise of atomic structures [77].

### 4.2. Theoretical Results and Discussion

Previously, first-principles DFT has been used to successfully calculate the electronic and magnetic properties of Heusler alloys [78–80]. In order to confirm experimental results and further investigate the electronic structure of this particular  $\text{Fe}_{3-x}\text{V}_x\text{Ge}$  alloy system, we employed the Special Quasi-random Structures (SQS) method to generate structures between  $x = 0$  and  $x = 1$  for the  $\text{L2}_1$  and  $\text{DO}_{19}$  phases. When comparing with experiment, we were able to generate structures with all of the same alloying ratios as Table 3 except  $x = 0.40$  for the  $\text{L2}_1$  phase. We note that for certain alloying ratios for the  $\text{L2}_1$  phase such as  $x = 0.375$ ,  $x = 0.40$ , and  $x = 0.625$ , the SQS method requires a larger supercell

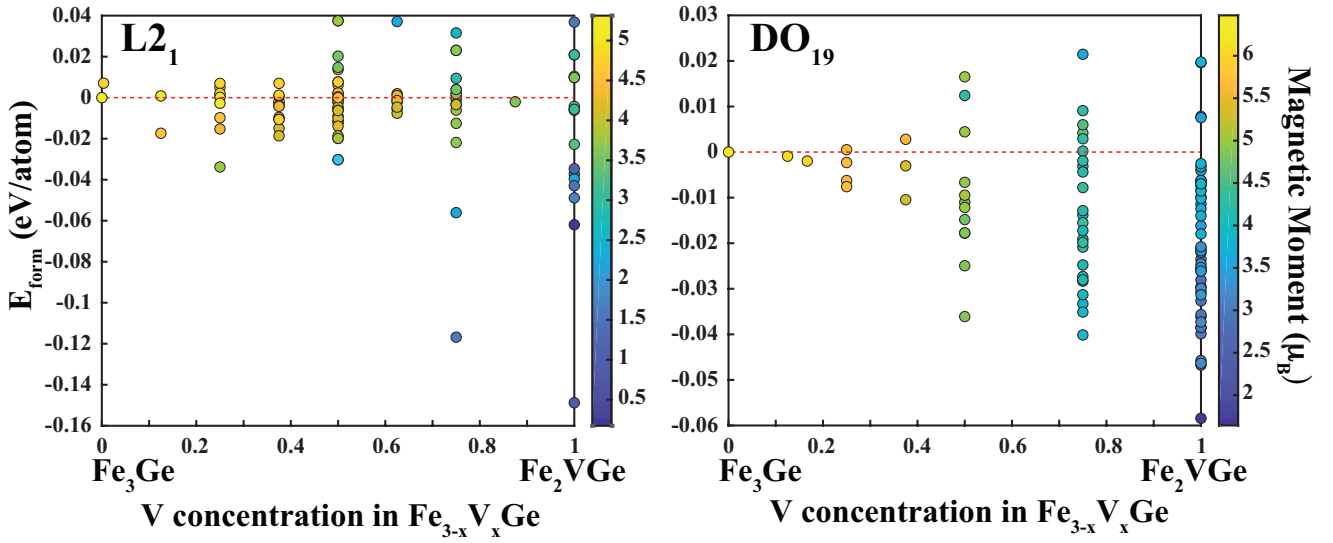


**Figure 11:** (color online) The formation energy (in eV/atom) as a function of V concentration for the  $\text{L2}_1$  and  $\text{DO}_{19}$  alloys created with the SQS method. Each data point represents a different structure and the color axis indicates the magnetic moment value for each structure.

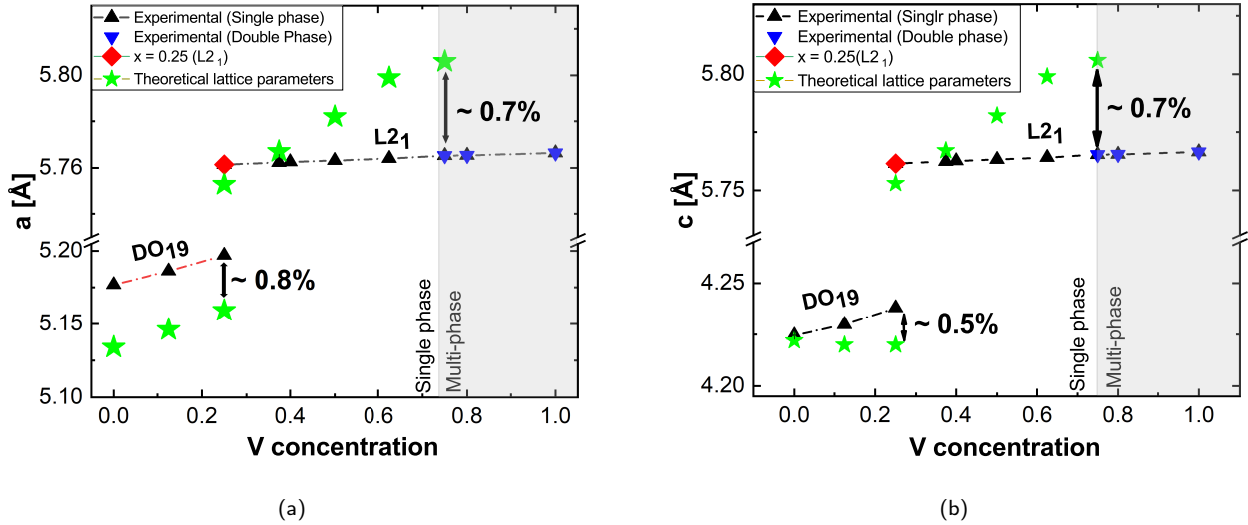


**Figure 12:** (color online) Comparison plot between experimentally extracted lattice parameters and theoretical values from First-principles calculations of  $\text{Fe}_{3-x}\text{V}_x\text{Ge}$  (a)  $a$  versus V concentration, and (b)  $c$  versus V concentration.

to preserve such concentrations. We propose that the SQS method being unable to create structures near  $x = 0.40$  is due to the requirement of a significantly large supercell, beyond the capability of DFT. For  $x = 0.375$  and  $x = 0.625$ , the quasi-random structures are forced to be confined to a rectangular supercell rather than a cubic supercell to preserve such alloying ratios without approaching the DFT limit (a much larger cubic supercell). However, from these rectangular structures, we are still able to obtain accurate lattice parameters to compare with experiment where only the long edges of the rectangular cell ( $b$ ) are almost two times larger than the ( $a$ ) lattice constant.

FIG 11 shows the formation energy as a function of V concentration  $x$  of the  $\text{L2}_1$  and  $\text{DO}_{19}$  phases respectively. The magnetic moment value is also depicted in the color axis of FIG 11. We observe that at  $x = 0.25$ , the  $\text{L2}_1$  phase is more energetically favourable than the  $\text{DO}_{19}$  phase. As expected for both phases, the increase of V concentration results in a decrease in magnetic moment with  $\text{Fe}_2\text{VGe}$  ( $x = 1$ ) being the least magnetic alloying concentration. As can be seen in Table 3, calculated magnetic moments are in good agreement with the experimentally measured values. The calculated values of magnetic moment for  $x = 0.375$  ( $M_{S,avg} = 4.48 \mu_B$ ) and  $x = 0.625$  ( $M_{S,avg} = 3.61 \mu_B$ ) are almost 1



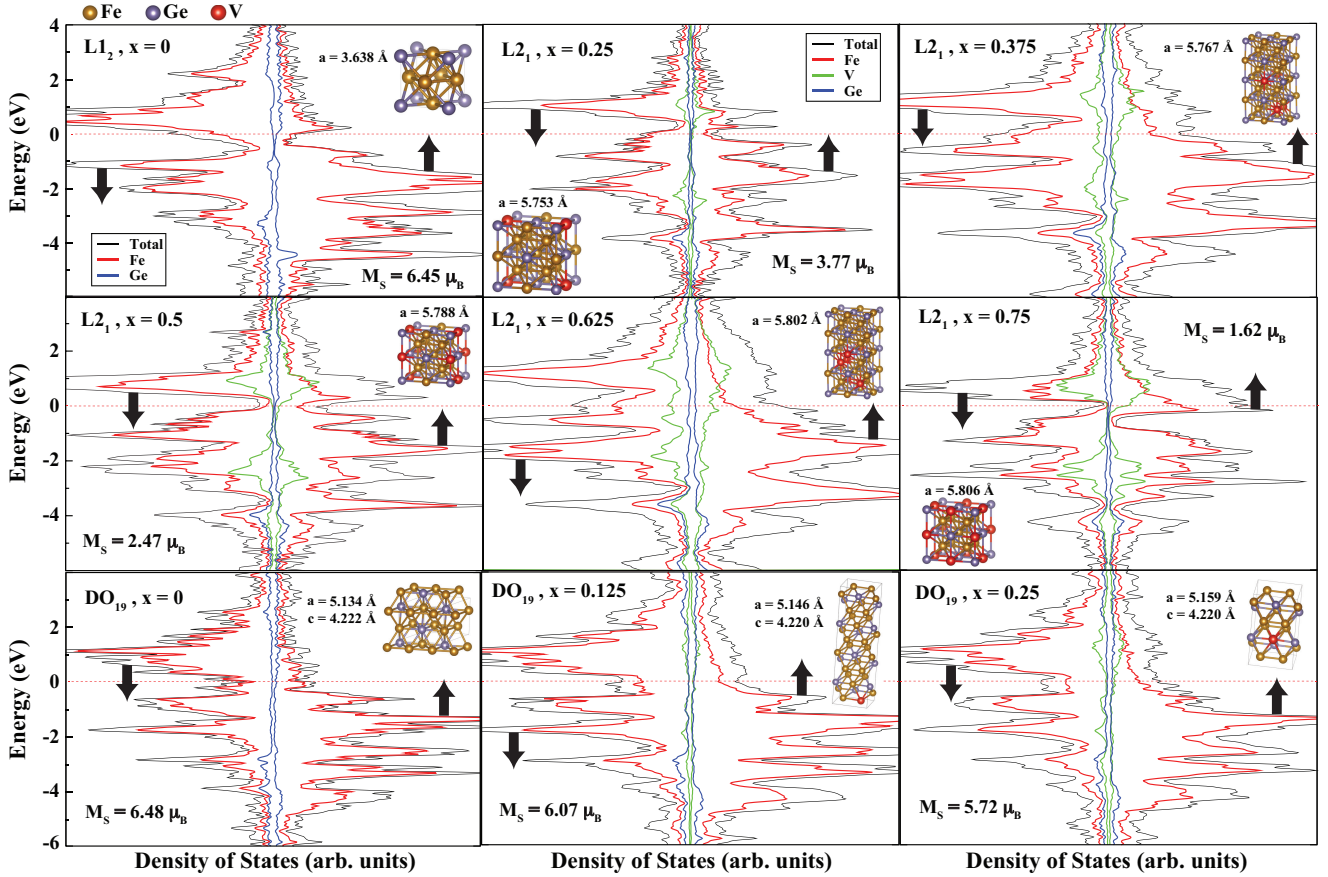


**Figure 13:** (color online) The DOS and PDOS of the lowest energy structure at specific concentration ratios for  $\text{L2}_1$ ,  $\text{DO}_{19}$ , and  $\text{L1}_2$ . The black arrows depict the spin up and spin down contributions and the red dotted line represents the Fermi level. The figure insets include the optimised structures, magnetic moment values and average lattice constants.

$\mu_B$  bigger than the experimental results due to considered supercells being rectangular instead of cubic. For the lowest energy structure (most energetically favourable) at each experimentally observed alloying concentration, we calculated the electronic density of states (DOS). FIG 13 depicts the atom projected DOS of the experimentally observed alloys for  $\text{L2}_1$  ( $x = 0.25, x = 0.375, x = 0.50, x = 0.625, x = 0.75$ ),  $\text{DO}_{19}$  ( $x = 0, x = 0.125, x = 0.25$ ) and  $\text{L1}_2$  ( $x = 0$ ). The spin up and spin down contributions to the DOS are indicated by the black arrows. The insets of FIG 13 also include the optimised geometry, the lattice constants and magnetic moment values (excluding  $M_s$  for  $x = 0.375$  and  $x = 0.625$ ) for the considered alloys. All the experimentally extracted lattice parameters are within  $\sim 1\%$  of theoretical values (see FIG 12). Because the experiments were done at a finite temperatures, this can cause the lattice parameters of the crystal structure to change from the 0 K structures due to the thermal expansion coefficient of the material and one might need longer annealing time yet to reach the true ground state. This also creates a margin of error such that all the structures generated with SQS lie in the range of thermal fluctuation at a given concentration. Due to this fact, we report an average value for lattice constant given at each concentration. In comparison to experiment, DFT calculations confirm that in-

creasing V concentration increases the lattice constant on average (see FIG 12). The metallic characteristics of the  $\text{DO}_{19}$  and  $\text{L1}_2$  (for  $x = 0$ )  $\text{Fe}_3\text{Ge}$  structures arise from the orbital contribution of Fe atoms. Vanadium substitution can give different contributions to the density of states according to its position inside the material. For instance, if the V atom is positioned close to Ge atoms, it gives a contribution similar to the Ge contribution (see FIG 13  $\text{L2}_1$  for  $x = 0.50$ , and  $x = 0.75$ ). When V atoms are placed far from the Ge atoms, specifically if they are surrounded by Fe atoms, their DOS look similar to the DOS of Fe atoms (see FIG 13  $\text{L2}_1$  for  $x = 0.375, x = 0.50$ , and  $x = 0.625$ ). For the  $\text{DO}_{19}$  structures, V atom substitution does not significantly effect the DOS of the bare  $\text{Fe}_3\text{Ge}$  structure due to low V concentration.

To understand the bonding type between the atoms and to gain insight on the electronic mechanism of these structures, we performed Bader charge transfer analysis of the  $\text{Fe}_{3-x}\text{V}_x\text{Ge}$  alloys. Bader charge analysis indicates that while 0.10 electrons ( $e^-$ ) transfer to Ge from Fe atoms for  $\text{L1}_2$ , 0.30  $e^-$  transfer for  $\text{DO}_{19}$  at  $x = 0$ . This amount of electron transfer, in addition to the electronegativity difference between Fe and Ge atoms (0.18 according to the Pauling scale) indicate that there is non-polar covalent bonding between them. For  $\text{DO}_{19}$  at  $x = 0.125$  and  $x = 0.25$ , V (which

has a lower electronegativity than Fe and Ge) loses  $1.38 e^-$  and the three Ge atoms that are binding with this V atom gain  $0.50 e^-$ . Bader charge analysis for  $\text{L2}_1$  at  $x = 0$  indicates that charge transfer is different from  $\text{DO}_{19}$  and  $\text{L1}_2$  structures. Some Fe atoms which are binding with Ge donate  $0.30 e^-$  and each Ge atoms take  $0.13 e^-$  while some Fe atoms take  $0.07 e^-$ . With the substitution of V atoms instead of Fe atoms, polarisation increases between the Fe atoms. For  $x = 0.50$ , Fe atoms that are close to Ge atoms donate  $0.35 e^-$  while the remaining Fe atoms gain  $0.35 e^-$ . The increasing of stability can be attributed to this increased polarisation.

## 5. Conclusion

In summary, an off-stoichiometric polycrystalline bulk  $\text{Fe}_{3-x}\text{V}_x\text{Ge}$  intermetallic alloys series ( $0 \leq x \leq 1$ ) was synthesised by arc-melting and the structural, magnetic, electrical transport and mechanical properties were investigated under different heat-treatment conditions. V substitution was observed to favour one of the Fe site in  $\text{Fe}_3\text{Ge}$  energetically to form  $\text{L2}_1$  structure for higher V concentration and  $\text{DO}_{19}$  structure for lower V concentrations, corroborated by first-principles calculations. The  $\text{L2}_1$  to  $\text{DO}_{19}$  martensitic phase transformation was observed to depend on V concentration as well as annealing conditions. DSC results also confirmed the diffusionless martensitic phase transformation in the alloy series. All the alloys in the series were found to be soft ferromagnets at 5 K with decreasing saturation magnetic moment with increasing V concentration. The sample with  $x = 0.25$  crystallised in two different crystal structures  $\text{L2}_1$  and  $\text{DO}_{19}$  at two different annealing conditions, and they were found to exhibit two different saturation magnetisations at 5 K, with the magnetisation in the hexagonal phase being substantially larger. In contrast to  $\text{DO}_{19}$  structures, the saturation magnetic moments of all  $\text{L2}_1$  structures were observed to decrease linearly with V concentration in close agreement with the expected Slater-Pauling values. The hexagonal samples were in all cases observed to have markedly higher values of saturation moments. The saturation magnetic moments extracted from experiment are found to be in good agreement with those obtained from first-principles calculations. The ferromagnetic Curie temperature  $T_c$  of these alloys were observed to decrease with increasing V concentration. The electrical resistivity measured over the temperature range from 5 K to 400 K showed a negative temperature coefficient of resistivity at high temperatures, more so with increasing the V concentration. The residual resistivity value is also found to increase with V substitution. Relatively high mechanical hardness values are also measured, increasing as V content increased. Vanadium is found to play a central role in tuning rich physical properties in  $\text{Fe}_{3-x}\text{V}_x\text{Ge}$ , changing the mechanical properties, stabilising the  $\text{L2}_1$  structure not found in the parent  $\text{Fe}_3\text{Ge}$  compound, and shifting the martensitic transformation temperature to higher values compared to that of parent  $\text{Fe}_3\text{Ge}$ .

## Acknowledgments

We would like to acknowledge Dr. Mark Weaver for helpful discussions on measurements of mechanical properties and for providing the instrument for hardness measurements. We would also like to acknowledge Mr. Bibekananda Das for helping us in carrying out high temperature magnetisation measurements. This work utilises the facilities offered by Central Analytical Facility (CAF) and MINT center of University of Alabama. We are thus grateful to the members of CAF and MINT center for helping us with measurements. The computational resources were provided by the UMBC High Performance Computing Facility (HPCF). The financial support to conduct this work was sourced from NSF DMREF Grant number 1235396, NSF DMR Grant number 1508680 and NSF DMR Grant number 1726213. The authors are thankful to NSF for providing the support to carry out this work.

## References

- [1] F. Heusler, Über magnetische manganlegierungen., Verhandlungen der Deutschen physikalischen Gesellschaft 5 (1903) 219.
- [2] C. Felser, G. H. Fecher, Spintronics: from materials to devices, Springer Science & Business Media, 2013.
- [3] F. Casper, C. Felser, R. Seshadri, C. P. Sebastian, R. Pöttgen, Searching for hexagonal analogues of the half-metallic half-Heusler XYZ compounds, Journal of Physics D: Applied Physics 41 (3) (2008) 035002.
- [4] T. Graf, C. Felser, S. S. Parkin, Simple rules for the understanding of Heusler compounds, Progress in solid state chemistry 39 (1) (2011) 1–50.
- [5] S. A. Khandy, D. C. Gupta, DFT investigations on mechanical stability, electronic structure and magnetism in  $\text{Co}_2\text{TaZ}$  ( $Z = \text{Al, Ga, In}$ ) heusler alloys, Semiconductor Science and Technology 32 (12) (2017) 125019.
- [6] L. Fan, F. Chen, C.-m. Li, X. Hou, X. Zhu, J.-l. Luo, Z.-Q. Chen, Promising spintronics: Mn-based Heusler alloys  $\text{Mn}_3\text{Ga}$ ,  $\text{Mn}_2\text{YGa}$  ( $Y = \text{V, Nb, Ta}$ ),  $\text{ScMnVGa}$ , Journal of Magnetism and Magnetic Materials 497 (2020) 166060.
- [7] Q. Zhang, H. Cui, C. Tian, H. Chen, J. Wang, H. Yuan, Thickness and composition dependencies of magnetization and perpendicular magnetic anisotropy of Heusler-like alloys based  $\text{Mn}_x\text{Ga}$   $\text{Co}_2\text{FeAl}$  superlattices, Journal of Alloys and Compounds 773 (2019) 327–337.
- [8] K. V. Shanavas, M. A. McGuire, D. S. Parker, Electronic and magnetic properties of Si substituted  $\text{Fe}_3\text{Ge}$ , Journal of Applied Physics 118 (12) (2015) 123902.
- [9] Y. Sakuraba, K. Izumi, T. Iwase, S. Bosu, K. Saito, K. Takanashi, Y. Miura, K. Futatsukawa, K. Abe, M. Shirai, Mechanism of large magnetoresistance in  $\text{Co}_2\text{MnSi}/\text{Ag}/\text{Co}_2\text{MnSi}$  devices with current perpendicular to the plane, Phys. Rev. B 82 (2010) 094444.
- [10] T. Nakatani, N. Hase, H. Goripati, Y. Takahashi, T. Furubayashi, K. Hono, Co-based Heusler alloys for CPP-GMR spin-valves with large magnetoresistive outputs, IEEE Transactions on Magnetics 48 (5) (2012) 1751–1757.
- [11] K. Yakushiji, K. Saito, S. Mitani, K. Takanashi, Y. Takahashi, K. Hono, Current-perpendicular-to-plane magnetoresistance in epitaxial  $\text{Co}_2\text{MnSi}/\text{Cr}/\text{Co}_2\text{MnSi}$  trilayers, Applied physics letters 88 (22) (2006) 222504.
- [12] M. Kratochvílová, D. Král, M. Dušek, J. Valenta, R. Colman, O. Heczko, M. Veis,  $\text{Fe}_2\text{MnSn}$ -experimental quest for predicted heusler alloy, Journal of Magnetism and Magnetic Materials (2020) 166426.
- [13] F. Xin, C. You, H. Fu, L. Ma, Z. Cheng, N. Tian, Mechanically tuning magnetism and transport property in spin gapless semiconductor

- CoFeMnSi flexible thin film, *Journal of Alloys and Compounds* 813 (2020) 152207.
- [14] T. Hahn, The 230 space groups, in: *International Tables for Crystallography Volume A: Space-Group Symmetry*, Springer, 2006, pp. 112–717.
  - [15] M. J. Mehl, D. Hicks, C. Toher, O. Levy, R. M. Hanson, G. Hart, S. Curtarolo, The AFLOW library of crystallographic prototypes: part 1, *Computational Materials Science* 136 (2017) S1–S828.
  - [16] X. Wang, Z. Cheng, Y. Jin, Y. Wu, X. Dai, G. Liu, Magneto-electronic properties and tetragonal deformation of rare-earth-element-based quaternary heusler half-metals: A first-principles prediction, *Journal of Alloys and Compounds* 734 (2018) 329–341.
  - [17] S. Keshavarz, N. Naghibolashrafi, M. E. Jamer, K. Vinson, D. Mazumdar, C. L. Dennis, W. Ratcliff II, J. A. Borchers, A. Gupta, P. LeClair,  $\text{Fe}_2\text{MnGe}$ : A hexagonal Heusler analogue, *Journal of Alloys and Compounds* 771 (2019) 793–802.
  - [18] A. F. Cabrera, F. H. Sánchez, Mössbauer study of ball-milled Fe-Ge alloys, *Phys. Rev. B* 65 (2002) 094202.
  - [19] Q. Chen, A. Ngan, B. Duggan, An in-situ TEM study of the  $\text{L}_{12}$  to  $\text{DO}_{19}$  phase transformation in the intermetallic compound  $\text{Fe}_3\text{Ge}$ , *Intermetallics* 6 (2) (1998) 105–114.
  - [20] Q. Chen, A. Ngan, B. Duggan, The  $\text{L}_{12} \rightarrow \text{DO}_{19}$  transformation in the intermetallic compound  $\text{Fe}_3\text{Ge}$ , *Journal of materials science* 33 (22) (1998) 5405–5414.
  - [21] J. Drijver, S. Sinnema, F. Van der Woude, Magnetic properties of hexagonal and cubic  $\text{Fe}_3\text{Ge}$ , *Journal of Physics F: Metal Physics* 6 (11) (1976) 2165.
  - [22] H. Nakagawa, K. Kanematsu, Magnetic and X-Ray studies on  $(\text{Fe}_{1-x}\text{V}_x)_3\text{Ge}$ , *Japanese Journal of Applied Physics* 18 (10) (1979) 1959.
  - [23] A. Beitollahi, J. Booth, Structural and magnetic properties of  $\text{Fe}_{3-x}\text{V}_x\text{Ge}$  alloys, *Journal of Physics: Condensed Matter* 2 (13) (1990) 2997.
  - [24] K. v. Buschow, P. Van Engen, R. Jongebreur, Magneto-optical properties of metallic ferromagnetic materials, *Journal of magnetism and magnetic materials* 38 (1) (1983) 1–22.
  - [25] P. Walker, W. H. Tarn, *CRC handbook of metal etchants*, CRC press, 1990.
  - [26] C. Boudias, D. Monceau, *CaRIne Crystallography: The Crystallographic Software for Research and Teaching*, CaRIne Crystallography, 2006.
  - [27] P. LeClair, X-ray Diffraction Calculation Software. (2018) <http://pleclair.ua.edu/XRD/>.
  - [28] A. Putz, H. Brandenburg, Phase Identification from Power Diffraction, *Crystal Impact Kreuzherrenstr. 102, 53227 Bonn, Germany* <https://www.crystalimpact.de/match>.
  - [29] H. S. Nalwa, *Handbook of nanostructured materials and nanotechnology*, five-volume set, Academic Press, 1999.
  - [30] S. KC, R. Mahat, S. Regmi, A. Mukherjee, P. Padhan, R. Datta, W. H. Butler, A. Gupta, P. LeClair, Tunable properties and potential half-metallicity in  $(\text{Co}_{2-x}\text{Ti}_x)\text{FeGe}$  Heusler alloys: An experimental and theoretical investigation, *Phys. Rev. Materials* 3 (2019) 114406.
  - [31] M. Mohammadtaheri, A new metallographic technique for revealing grain boundaries in aluminum alloys, *Metallography, Microstructure, and Analysis* 1 (5) (2012) 224–226.
  - [32] Y. El Hachi, B. Malard, S. Berveiller, J. Wright, Measurement of lattice rotations and internal stresses in over one hundred individual grains during a stress-induced martensitic transformation, in: *MATEC Web of Conferences*, Vol. 33, EDP Sciences, 2015, p. 02003.
  - [33] H. P. Wijn, *Magnetic Properties of Metals: d-elements, alloys and Compounds*, Springer Science & Business Media, 2012.
  - [34] B. Cullity, S. Stock, *Elements of X-ray Diffraction*, pp (2014).
  - [35] A. R. Denton, N. W. Ashcroft, Vegard's law, *Phys. Rev. A* 43 (1991) 3161–3164.
  - [36] J. R. Rumble, *CRC Handbook of Chemistry and Physics 100th Edition* (Internet Version 2019) CRC Press.
  - [37] Z. Nishiyama, *Martensitic transformation*, Elsevier, 2012.
  - [38] R. M. Wentzcovitch, P. K. Lam, fcc-to-hcp transformation: A first-principles investigation, *Phys. Rev. B* 44 (1991) 9155–9158.
  - [39] K. Manna, Y. Sun, L. Muechler, J. Kübler, C. Felser, Heusler, weyl and berry, *Nature Reviews Materials* 3 (8) (2018) 244.
  - [40] T. Kaneko, T. Kanomata, Y. Kawazoe, Y. Uwatoko, *Magnetic Properties of d-Elements, Alloys and Compounds Under Pressure*, Springer, 2014.
  - [41] A. Arrott, Criterion for ferromagnetism from observations of magnetic isotherms, *Phys. Rev.* 108 (1957) 1394–1396.
  - [42] S. Wurmehl, G. H. Fecher, H. C. Kandpal, V. Ksenofontov, C. Felser, H.-J. Lin, Investigation of  $\text{Co}_2\text{FeSi}$ : The Heusler compound with highest Curie temperature and magnetic moment, *Applied physics letters* 88 (3) (2006) 032503.
  - [43] L. J. van der Pauw, A method of measuring specific resistivity and hall effect of discs of arbitrary shape, *Philips Res. Rep* 13 (1) (1958) 1–9.
  - [44] P. L. Rossiter, *The electrical resistivity of metals and alloys*, Vol. 6, Cambridge University Press, 1991.
  - [45] P. Allen, B. Chakraborty, Infrared and dc conductivity in metals with strong scattering: nonclassical behavior from a generalized boltzmann equation containing band-mixing effects, *Physical Review B* 23 (10) (1981) 4815.
  - [46] Y. Nishino, M. Kato, S. Asano, K. Soda, M. Hayasaki, U. Mizutani, Semiconductorlike behavior of electrical resistivity in Heusler-type  $\text{Fe}_2\text{VAl}$  compound, *Phys. Rev. Lett.* 79 (1997) 1909–1912.
  - [47] C.-S. Lue, Y.-K. Kuo, Thermal and transport properties of the Heusler-type compounds  $\text{Fe}_{2-x}\text{Ti}_{1+x}\text{Sn}$ , *Journal of applied physics* 96 (5) (2004) 2681–2683.
  - [48] N. Kawamiya, Y. Nishino, M. Matsuo, S. Asano, Electrical-resistance maximum near the Curie point in  $(\text{Fe}_{1-x}\text{V}_x)_3\text{Ga}$  and  $(\text{Fe}_{1-x}\text{Ti}_x)_3\text{Ga}$ , *Phys. Rev. B* 44 (1991) 12406–12412.
  - [49] C. S. Lue, Y.-K. Kuo, Thermoelectric properties of the semimetallic Heusler compounds  $\text{Fe}_{2-x}\text{V}_{1+x}\text{M}$  ( $\text{M} = \text{Al, Ga}$ ), *Phys. Rev. B* 66 (2002) 085121.
  - [50] N. Kourov, A. Korolev, V. Marchenkov, A. Lukoyanov, K. Belozero, Magnetic and electrical properties of the half-metallic ferromagnets  $\text{Co}_2\text{CrAl}$ , *Physics of the Solid State* 55 (5) (2013) 977–985.
  - [51] S. Majumdar, M. Chattopadhyay, V. Sharma, K. Sokhey, S. Roy, P. Chaddah, Transport properties of the ferromagnetic Heusler alloy  $\text{Co}_2\text{TiSn}$ , *Physical Review B* 72 (1) (2005) 012417.
  - [52] J. Barth, G. H. Fecher, B. Balke, S. Ouardi, T. Graf, C. Felser, A. Shk-abko, A. Weidenkaff, P. Klaer, H. J. Elmers, et al., Itinerant half-metallic ferromagnets  $\text{Co}_2\text{TiZ}$  ( $\text{Z} = \text{Si, Ge, Sn}$ ): Ab initio calculations and measurement of the electronic structure and transport properties, *Physical Review B* 81 (6) (2010) 064404.
  - [53] N. Kourov, V. Marchenkov, V. Pushin, K. Belozero, Electrical properties of ferromagnetic  $\text{Ni}_2\text{MnGa}$  and  $\text{Co}_2\text{CrGa}$  Heusler alloys, *Journal of Experimental and Theoretical Physics* 117 (1) (2013) 121–125.
  - [54] N. Kourov, A. Lukoyanov, V. Marchenkov, Specific features of the electrical resistance of half-metallic ferromagnetic alloys  $\text{Co}_2\text{CrAl}$  and  $\text{Co}_2\text{CrGa}$ , *Physics of the Solid State* 55 (12) (2013) 2487–2490.
  - [55] N. Kourov, V. Marchenkov, K. Belozero, H. Weber, Specific features of the electrical resistivity of half-metallic ferromagnets  $\text{Fe}_2\text{MeAl}$  ( $\text{Me} = \text{Ti, V, Cr, Mn, Fe, Ni}$ ), *Journal of Experimental and Theoretical Physics* 118 (3) (2014) 426–431.
  - [56] H. Kurt, K. Rode, P. Stamenov, M. Venkatesan, Y.-C. Lau, E. Fonda, J. Coey, Cubic  $\text{Mn}_2\text{Ga}$  thin films: Crossing the spin gap with ruthenium, *Physical review letters* 112 (2) (2014) 027201.
  - [57] L. Jodin, J. Tobola, P. Pecher, H. Scherrer, S. Kaprzyk, Effect of substitutions and defects in half-heusler  $\text{FeVSb}$  studied by electron transport measurements and kkr-cpa electronic structure calculations, *Phys. Rev. B* 70 (2004) 184207.
  - [58] M. I. Khan, H. Arshad, M. Rizwan, S. Gillani, M. Zafar, S. Ahmed, M. Shakil, Investigation of structural, electronic, magnetic and mechanical properties of a new series of equiatomic quaternary Heusler alloys  $\text{CoYCrZ}$  ( $\text{Z} = \text{Si, Ge, Ga, Al}$ ): A DFT study, *Journal of Alloys and Compounds* (2019) 152964.
  - [59] S. Yousuf, D. C. Gupta, Insight into half-metallicity, spin-polarization and mechanical properties of  $\text{L}_{21}$  structured  $\text{MnY}_2\text{Z}$  ( $\text{Z} = \text{Al, Si, Ga}$ ,



- Ge, Sn, Sb) Heusler alloys, *Journal of Alloys and Compounds* 735 (2018) 1245–1252.
- [60] M. Elahmar, H. Rached, D. Rached, R. Khenata, G. Murtaza, S. B. Omran, W. Ahmed, Structural, mechanical, electronic and magnetic properties of a new series of quaternary Heusler alloys  $\text{CoFeMnZ}$  ( $Z = \text{Si, As, Sb}$ ): a first-principle study, *Journal of Magnetism and Magnetic Materials* 393 (2015) 165–174.
- [61] K. Benkaddour, A. Chahed, A. Amar, H. Rozale, A. Lakdja, O. Benhelal, A. Sayede, First-principles study of structural, elastic, thermodynamic, electronic and magnetic properties for the quaternary Heusler alloys  $\text{CoRuFeZ}$  ( $Z = \text{Si, Ge, Sn}$ ), *Journal of Alloys and Compounds* 687 (2016) 211–220.
- [62] L. Zhang, X. Wang, Z. Cheng, Electronic, magnetic, mechanical, half-metallic and highly dispersive zero-gap half-metallic properties of rare-earth-element-based quaternary heusler compounds, *Journal of Alloys and Compounds* 718 (2017) 63–74.
- [63] K.-D. Kim, C.-H. Lee, Fabrication and densification of Heusler  $\text{Fe}_2\text{VAl}$  alloy powders by mechanical alloying, *Journal of the Korean Crystal Growth and Crystal Technology* 23 (1) (2013) 51–57.
- [64] M. Hakimi, P. Kameli, H. Salamati, Y. Mazaheri, Evolution of microstructural and mechanical properties of nanocrystalline  $\text{Co}_2\text{FeAl}$  Heusler alloy prepared by mechanical alloying, *Powder Metallurgy* 56 (2) (2013) 111–116.
- [65] S. Ouardi, G. H. Fecher, B. Balke, A. Beleanu, X. Kozina, G. Stryganyuk, C. Felser, W. Klöß, H. Schrader, F. Bernardi, J. Morais, E. Ikenaga, Y. Yamashita, S. Ueda, K. Kobayashi, Electronic and crystallographic structure, hard x-ray photoemission, and mechanical and transport properties of the half-metallic Heusler compound  $\text{Co}_2\text{MnGe}$ , *Phys. Rev. B* 84 (2011) 155122.
- [66] G. Rogl, A. Grytsiv, M. Gürth, A. Tavassoli, C. Ebner, A. Wünschek, S. Puchegger, V. Soprunyuk, W. Schranz, E. Bauer, et al., Mechanical properties of half-Heusler alloys, *Acta Materialia* 107 (2016) 178–195.
- [67] Z. Xie, S. Ni, M. Song, Effect of  $\text{Y}_2\text{O}_3$  doping on FCC to HCP phase transformation in cobalt produced by ball milling and spark plasma sintering, *Powder Technology* 324 (2018) 1–4.
- [68] G. Kresse, J. Furthmüller, Efficient iterative schemes for ab initio total-energy calculations using a plane-wave basis set, *Phys. Rev. B* 54 (1996) 11169–11186.
- [69] G. Kresse, D. Joubert, From ultrasoft pseudopotentials to the projector augmented-wave method, *Phys. Rev. B* 59 (1999) 1758–1775.
- [70] P. E. Blöchl, Projector augmented-wave method, *Phys. Rev. B* 50 (1994) 17953–17979.
- [71] J. P. Perdew, K. Burke, M. Ernzerhof, Generalized gradient approximation made simple, *Phys. Rev. Lett.* 77 (1996) 3865–3868.
- [72] H. J. Monkhorst, J. D. Pack, Special points for brillouin-zone integrations, *Phys. Rev. B* 13 (1976) 5188–5192.
- [73] A. Zunger, S.-H. Wei, L. G. Ferreira, J. E. Bernard, Special quasirandom structures, *Phys. Rev. Lett.* 65 (1990) 353–356.
- [74] A. van de Walle, Multicomponent multisublattice alloys, nonconfigurational entropy and other additions to the alloy theoretic automated toolkit, *Calphad* 33 (2) (2009) 266–278.
- [75] R. F. W. Bader, *Atoms in Molecules*, American Cancer Society, 2002.
- [76] G. Henkelman, A. Arnaldsson, H. Jónsson, A fast and robust algorithm for bader decomposition of charge density, *Computational Materials Science* 36 (3) (2006) 354–360.
- [77] K. Momma, F. Izumi, Vesta 3 for three-dimensional visualization of crystal volumetric and morphology data, *Journal of Applied Crystallography* 44 (6) (2011) 1272–1276.
- [78] Y. Zhang, Z. Liu, Z. Wu, X. Ma, Prediction of fully compensated ferrimagnetic spin-gapless semiconducting  $\text{FeMnGa/Al/In}$  half Heusler alloys, *IUCrJ* 6 (4).
- [79] T. Samanta, S. Chaudhuri, S. Singh, V. Srihari, A. Nigam, P. Bhobe, Structural, electronic, magnetic, and transport properties of the equiatomic ni-based quaternary heusler alloys, *Journal of Alloys and Compounds* (2019) 153029.
- [80] A. Candan, G. Uğur, Z. Charifi, H. Baaziz, M. Ellialtıoğlu, Electronic structure and vibrational properties in cobalt-based full-Heusler compounds: A first principle study of  $\text{Co}_2\text{MnX}$  ( $X = \text{Si, Ge, Al, Ga}$ ), *Journal of Alloys and Compounds* 560 (2013) 215–222.